Bioengineering fascicle-like skeletal muscle bioactuators via pluronic-assisted co-axial 3D bioprinting (PACA-3D)

To cite this article: Judith Fuentes *et al* 2025 *Biofabrication* **17** 035018

Biofabrication

PAPER

Bioengineering fascicle-like skeletal muscle bioactuators via pluronic-assisted co-axial 3D bioprinting (PACA-3D)

Judith Fuentes[1,7], **Rafael Mestre**[1,2,7,*], **Maria Guix**[1,3,*], **David Esporrín-Ubieto**[1], **Ibtissam Ghailan Tribak**[1,4], **Noelia Ruiz-González**[1], **Tania Patiño**[1,5] and **Samuel Sánchez**[1,6,*]

[1] Institute for Bioengineering of Catalonia (IBEC), Barcelona Institute of Science and Technology (BIST), Baldiri-Reixac 10-12, 08028 Barcelona, Spain
[2] School of Electronics and Computer Science, University of Southampton, Highfield SO17 1BJ, United Kingdom
[3] Department of Materials Science and Physical Chemistry, Institute of Theoretical and Computational Chemistry, University of Barcelona, 08028 Barcelona, Spain
[4] ICFO—Institut de Ciències Fotòniques, The Barcelona Institute of Science and Technology, Carl Friedrich Gauss, 3, Castelldefels, Barcelona 08860, Spain
[5] Biomedical Engineering Department, Institute for Complex Molecular Systems. Technische Universiteit Eindhoven, Het Kranenveld 14, 5612 AZ Eindhoven, The Netherlands
[6] Institució Catalana de Recerca i Estudis Avançats (ICREA), Passeig de Lluís Companys 23, 08010 Barcelona, Spain
[7] Contributed equally.
[*] Authors to whom any correspondence should be addressed.

E-mail: r.mestre@soton.ac.uk, maria.guix@ub.edu and ssanchez@ibecbarcelona.eu

Keywords: bioengineering, 3D bioprinting, muscle-based actuators, pluronic, co-axial printing

Supplementary material for this article is available online

OPEN ACCESS

RECEIVED
25 September 2024

REVISED
9 May 2025

ACCEPTED FOR PUBLICATION
23 May 2025

PUBLISHED
6 June 2025

Abstract

Advances in 3D bioprinting have opened new possibilities for developing bioengineered muscle models that can mimic the architecture and function of native tissues. However, current bioengineering approaches do not fully recreate the complex fascicle-like hierarchical organization of the skeletal muscle tissue, impacting on the muscle maturation due to the lack of oxygen and nutrient supply in the scaffold inner regions. A key challenge is the production of precise and width-controlled independent filaments that do not fuse during the printing process when subsequently extruded, ensuring the formation of fascicle-like structures. This study addresses the limitation of filament fusion by utilizing a pluronic-assisted co-axial 3D bioprinting system (PACA-3D) creates a physical confinement of the bioink during the extrusion process, effectively obtaining thin and independent printed filaments with controlled shapes. The use of PACA-3D enabled the fabrication of skeletal muscle-based bioactuators with improved cell differentiation and significantly increased force output, obtaining 3 times stronger bioengineered muscle when compared to bioactuators fabricated using conventional 3D extrusion bioprinting techniques, where a single syringe containing the bioink is used. The versatility of our technology has been demonstrated using different biomaterials, demonstrating its potential to develop more complex biohybrid tissue-based architectures with improved functionality, as well as aiming for better scalability and printing flexibility.

1. Introduction

The 3D bioprinting technique allows automated and fast-prototyping printing of cell-laden hydrogels with biomimetic designs resembling the 3D environment of native tissue [1, 2]. Opposed to two-dimensional cultures, 3D bioprinting provides three-dimensional environments that better recreate the *in vivo* conditions in biological models, leading to improved cell–cell interaction, division, and morphology [3]. Pneumatic-extrusion-based bioprinting is the most widely used method in biofabrication, exploring different biocompatible hydrogels that allow optimal cell distribution and interaction during the maturation process. This technique is based on the extrusion of a cell-laden hydrogel through a nozzle when controlled pressure is applied using materials with sufficient pseudoplastic or shear-thinning behavior,

which allows printing at lower pressures while protecting cells from high shear stress conditions [4]. Materials like alginate, gelatin, fibrinogen, hyaluronic acid, chitosan, poly(ethylene glycol) diacrylate, collagen, nanocellulose, decellularized ECM, and chemical modifications of gelatin methacrylate (GelMA) have been widely used alone or in combination with one another for their shear-thinning properties, stiffness modulation, and biocompatibility [2, 3, 5–7]. More complex structures can be achieved by bioprinting multiple materials in parallel, using for example polycaprolactone [8], polydimethylsiloxane (PDMS) [9–11], or pluronic acid [12, 13]. Finally, it is commonly used as a sacrificial material to obtain overhanging structures or to create vascular channels/-complex 3D structures, as it can be easily washed away with cold water or phosphate buffered saline (PBS). Other interesting examples in pneumatic-extrusion-based 3D bioprinting have explored the use of cartilage [14], neural tissue [15], cardiac [16], skin [17], as well as multiple cell bioprinting for myotendinous tissues [18].

Native skeletal muscle tissue presents an inherently three-dimensional hierarchical architecture composed of groups of fibers called bundles, which are later organized in fascicles to conform to the muscle structure. Therefore, any tissue model that aims to recreate its complexity must consider this three-dimensional configuration, either by following 3D-bioprinting techniques [19, 20] or mold casting [21]. One of the main challenges remains in overcoming the lack of oxygen and nutrient diffusion when generating thick cell constructs. Indeed, the oxygen diffusion limit within a tissue is approximately 200 μm [22], leading to a significant loss of output force due to the lower myotube density in the muscle bundle [23]. Moreover, the fascicle-like structure of native muscle has not been completely replicated through 3D bioprinting because of the challenge of generating independent filaments, as in common extrusion bioprinting approaches the filaments fuse during the printing process (i.e. layer by layer). Indeed, a pioneer work where pneumatic-extrusion-based 3D bioprinting was used for the fabrication of human-scale tissues with structural integrity, reported the problems associated with the lack of nutrient diffusion due to the fusion of the printed filaments and the need to integrate vascularity of their constructs [3]. In the same line, some examples of fascicle-like constructs generated using sacrificial molds and microfabrication techniques [24–26]. However, these techniques lack the versatility and automation of 3D bioprinting methods. Recent studies in 3D bioprinting of skeletal muscle constructs have focused on innovative photo-crosslinking techniques, enabling the *in situ* crosslinking of bioinks during extrusion [19, 20, 27]. This approach allows precise control over the width and shape of printed filaments, which is crucial for obtaining fascicle-like structures. Despite these benefits, its versatility is limited by the use of photocrosslinkable bioinks. An alternative to light-triggered cross-linking is the FRESH method, which allows the fabrication of width-controlled filaments by extruding bioinks in support baths of sacrificial polymers [28, 29]. One key aspect of this approach is that the bath dimensions must be proportional to the size of the final printed construct, which is especially important to consider when printing large structures.

Another widely implemented method is co-axial printing, which is used to obtain tubular structures and vascular scaffolds [30–32] and has also been demonstrated to allow the creation of fascicle-like tissues [33]. Indeed, Lee *et al* replicated muscle fascicles and the perimysium, surrounding them by 3D printing a core–shell structure consisting of a photocrosslinkable polymer mixture in which C2C12 cell aggregates suspended in the medium were encapsulated. The fabrication of multi-fascicle skeletal muscles using core–shell technology has also been demonstrated with a multi-barrel coaxial nozzle [34]. This method produces a large filament with the desired multifiber organization; however, it lacks precise control over the positioning of individual filaments within the construct, as all filaments are co-extruded simultaneously. Moreover, this approach may impose limitations on design flexibility and printability, particularly for more complex structures. Another interesting fast fabrication co-axial based approach to achieve highly-aligned muscle fibers is the rotary wet-spinning biofabrication process, achieving a continuous production of core–shell hydrogel filaments onto a cylindric drum that results in a circular muscle construct [35]. By exploiting the advantages posed by co-axial printing, it is possible to go beyond the fabrication of vascular-like and core–shell structures. In fact, it can be applied to fabricate individual non-hollow filaments of defined widths. During co-extrusion, sacrificial materials in the outer layers create a physical confinement, leading to the formation of fascicle-like structures with improved control over filament size and homogeneity. Indeed, the rotary wet-spinning co-axial printing was also used for the fabrication of circular muscle myo-substitutes for regenerative medicine purposes [36]. However, this technique do not provide a high degree of freedom in terms of printing complex designs of fascicle-like filaments, as the rotary wet-spinning set up only allows the fabrication of circular-shaped structures.

Despite all the advances reported by the techniques described above, there is still the need to develop a fabrication method that offers a versatile, simple and more scalable approach to bioprinting, allowing materials to be directly deposited onto dry or wet substrates if needed, thus providing greater flexibility in biofabrication. In this study, we propose a pluronic-assisted co-axial 3D bioprinting technique

(PACA-3D) as a novel, simple and universal method to obtain nonhollow individual filaments. This is achieved through the co-extrusion of pluronic acid (i.e. sacrificial material in the outer layer) and the bioink (in the inner layer) which creates a physical confinement during the extrusion process. This technique: (i) produces homogenous filaments with controlled widths down to 190 μm; (ii) generates individual filaments that do not fuse with each other, creating a fascicle-like structure that improves the biomimicry of the native skeletal muscle tissue; and (iii) is a flexible and universal bioprinting method, as it can potentially include different types of hydrogels and different crosslinking strategies, including collagen (one of the main components of the skeletal muscle ECM). This provides an alternative method with some benefits compared to other reported techniques like FRESH, as it does not need to use a sacrificial bath, giving more flexibility in terms of working space and the ability to print onto dry substrates. Furthermore, we tested their functionality as bioactuators by evaluating the force output at different maturation stages. We observed that the bioactuators fabricated using PACA-3D with a fascicle-like structure exhibited enhanced contractile behavior compared to those fabricated using conventional 3D bioprinting, envisioned here as a control printing system, where the bioink is extruded from a single syringe without co-extrusion of pluronic, resulting in no physical confinement of the bioink during extrusion. Therefore, such bioengineered tissues can be used to study muscle development, maturation, or healing [37–39], and as a drug testing platform for biomedical or cosmetic purposes [11, 40], as well as being of great interest to develop more complex untethered actuators and bio-hybrid soft robots [41–43].

2. Materials and methods

2.1. Fabrication of the co-axial nozzles

Co-axial nozzles were manually fabricated using different types of commercially available nozzles and tips. The inner nozzle, through which the cell-laden hydrogel was extruded, was a 200 μm (G27) plastic conical nozzle (Optimum® SmoothFlow™ tapered tips, Nordson®, ref. 7018417). The luer lock of this nozzle was left free to connect to the first bioprinting barrel, where the cell-laden hydrogel was loaded. The outer nozzle that covered the inner nozzle was a filtered P1000 pipette tip (LabClinics, ref. LAB1000ULFNL) cut approximately 5 cm from its end. The tip was trimmed to increase the diameter at the final point. The nozzles were assembled and glued together. When the glue was dry and the assembly was stable, a hot puncher was used to create a hole in the outer nozzle, approximately 1.5 cm from its end, with care not to create another hole in the internal nozzle. The secondary nozzle, where the pluronic flowed, was inserted into the hole. This secondary nozzle was a flexible polypropylene 800 μm nozzle (G18) from Nordson® (EFD® 7018138). Silicone tubing with 0.8 mm of diameter (Ibidi, ref. 10841) was attached to the external nozzle through a male elbow luer connector (Ibidi, ref. 10802). A 1.1 mm (19 G) nozzle (B. Braun Sterican®, ref. 4657799) was inserted through the other end of the tubing so that its luer lock connector could be connected to the second bioprinting barrel containing the pluronic acid.

2.2. Hydrogel fabrication

For the fabrication of the different combinations of hydrogels, the following materials were used: gelatin from porcine skin, type A (Sigma-Aldrich, G2500), fibrinogen from bovine plasma (Sigma-Aldrich, F8630) with thrombin from bovine plasma (Sigma-Aldrich, T4648) as crosslinker, Matrigel Basement™ membrane matrix (Corning®, 354234), sodium alginate (Sigma-Aldrich, W201502), GelMA with lithium phenyl-2,4,6-trimethylbenzoylphosphinate at 0.25% (wt/v) as photoinitiator (CELLINK®, LIK-3050 V-1), collagen type I high concentration (Corning®, 354249), and pluronic® F-127 powder (Sigma-Aldrich, P2443).

pluronic was dissolved at concentrations ranging from 30%–40% (wt/v) in Milli-Q water with CaCl2 (at molar concentrations ranging from 50 mM to 300 mM) under stirring in a refrigerator (4 °C) until fully dissolved. Hydrogels containing gelatin, alginate, and/or GelMA in the same composition were mixed together in PBS at the desired concentrations. If the hydrogel contained fibrinogen, this component was dissolved in PBS at a 2x concentration and then added to the hydrogel containing alginate and/or gelatin, also at a 2x concentration, to avoid pipetting this very viscous mixture. If the hydrogel also contained Matrigel, the concentrations were adjusted to achieve the desired concentrations, reducing the need for pipetting (for instance, at a 1:1:1 ratio or 2:1:1 ratio).

2.3. Pluronic-assisted co-axial 3D bioprinting

C2C12 mouse myoblasts were purchased from ATCC and maintained in growth medium (GM) consisting of high glucose Dullbecco's Modified Eagle's medium (DMEM; Gibco®) supplemented with 10% fetal bovine serum, 200 nM L-glutamine, and 1% penicillin/streptomycin, in at 37 °C and 5% CO2 atmosphere. Cells were harvested before reaching 80% confluence in Corning® T-75 flasks by using 0.25% (wt/v) Trypsin-0.53 mM ethylenediaminetetraacetic acid (EDTA) solution, centrifuged at 300 g for 5 min, and the pellet re-suspended at a concentration of 5×10^6 cells ml^{-1} in the hydrogel mixture at 37 °C. The cell-laden hydrogel was loaded into a 3 ml plastic syringe (Nordson®, ref. 7012085) coupled to the inner nozzle of the co-axial nozzle and kept at 4 °C for 5 min to induce gelatin gelation. Although temperature control was not applied during the extrusion process,

the bioink—pre-cooled to 4 °C—maintained consistent viscosity throughout the entire printing process. Pluronic was loaded while cold into a secondary barrel and left at RT to the gel beforehand. A CELLINK® Inkredible+ 3D bioprinter was used to bioprint the hydrogel filaments. The cell-laden hydrogel was inserted in the first cartridge and the pluronic barrel into the second barrel, and all the nozzles were connected as previously explained. The pressure for the pluronic barrel was kept between 250–350 kPa and adjusted manually, although these values were highly dependent on the diameter and length of the silicone tubing and the concentration of pluronic. For the hydrogel, the pressures were kept between 40–80 kPa, also adjusted manually, depending on the type of hydrogel. The designs were directly written in GCode using the open-source software Slic3r (v. 1.2.9), and the bioprinter was controlled with RepetierHost (v. 2.0.5). After 3D bioprinting, if the hydrogel contained fibrinogen, a solution of 1.67 U ml^{-1} of thrombin was added to the Petri dish for 10 min in a refrigerator at 4 °C. At this point, pluronic would dissolve, and fibrinogen crosslinks to form fibrin. After this, several washes with cold PBS were performed to completely remove pluronic. GM was then added, which consisted of high-glucose Dulbecco's modified Eagle's medium (DMEM; Gibco) supplemented with 10% fetal bovine serum (Gibco), 200 nM l-glutamine (Gibco), and 1% penicillin-streptomycin (Gibco) and 6-aminocaproic acid (ACA), a proteinase inhibitor that avoids degradation of fibrin-based hydrogels by cells. Then, the constructs were left in a cell incubator at 37 °C a 5% CO2 atmosphere. If the hydrogel contained Matrigel, the as-printed constructs were left in an incubator for at least 30 min without removing the pluronic. After this, a cold solution of PBS (or thrombin, if fibrinogen was also present in the mixture) was added to dissolve the pluronic after several washes. If the chemical confinement method based on alginate was used, and this material wanted to be removed, a solution of 20 mM EDTA (Sigma-Aldrich, E6758) adjusted with NaOH to pH 7, was added to the Petri dish after crosslinking for 5 min. After 2 d in GM, the media is changed to differentiation medium (DM) consisting of high-glucose DMEM containing 10% horse serum (Gibco), 200 nM l-glutamine, 1% penicillin-streptomycin, IGF-1 (50 ng ml^{-1} ; Sigma-Aldrich), and 1 mg ml^{-1} of ACA. Then, samples were maintained in DM, changing medium every two days.

2.4. Conventional extrusion-based 3D bioprinting

C2C12 cells were harvested following the protocol mentioned above and resuspended with a hydrogel, composed of 7% (wt/v) gelatin and 4% (wt/v) fibrinogen, at a concentration of 5×10^6 cells ml^{-1} . The cell-laden bioink was loaded into a 3-ml plastic syringe (Nordson®, ref. 7012085) coupled to a 200 μm (G27) plastic conical nozzle, identical to the inner nozzle used in the PACA-3D system. The syringe was pre-cooled at 4 °C for 5 min to induce gelatin gelation and achieve the appropriate viscosity for extrusion. As in PACA-3D printing, no temperature control was applied in printing head during the printing process in conventional printing. The same design was used for both conventional and PACA-3D printing; however, in conventional printing, only the syringe containing the bioink was extruded, without the co-extrusion of bioink and pluronic as in PACA-3D. The printing pressure was maintained between 50–90 kPa, manually adjusting it when needed. After 3D bioprinting, a solution of 1.67 U ml^{-1} of thrombin was added to the Petri dish for 7 min to induce fibrinogen crosslinking. Gelatin was not crosslinked as it was used as a viscosity modulator. After this, several washes with PBS were performed and growth medium supplemented ACA was added, and the constructs were maintained in a cell incubator at 37 °C a 5% CO_2 atmosphere. After two days, samples were switched to differentiation medium with ACA being replaced with fresh medium every two days.

2.5. Rheological characterization of pluronic acid

The rheological characterization of pluronic was performed using a Discovery HR-2 controlled-stress rheometer (TA Instruments) equipped with a Peltier steel cone geometry with a diameter of 40 mm, 26 μm of truncation, and angle of 1.019°. The Peltier element was set to 4 °C and 25 °C to demonstrate the behavior of the block copolymer at low and room temperatures. In all experiments, the sample was left to acquire the desired temperature for 1 min. A flow ramp with a shear rate from 100 1 s^{-1} to 0.01 1 s^{-1} was performed in logarithmic mode with 600 s of duration per point, with pre-conditioning to a temperature of 30 s and pre-shear of 3 rad s^{-1} for 10 s.

2.6. Rheological characterization of bioinks

The rheological properties of various bioink compositions have been evaluated using an Anton Paar rheometer MCR 702, equipped with an upper disk of 40 mm diameter and 1° angle (CP40-1) with a fixed working gap of 0.078 mm. Flow curves from figures 2(C) and 3(A) have been performed at 18 °C. Stock solutions of each component were prepared based on the required final volume for analysis (350–400 μL), ensuring that the concentration of each component remained consistent in the final mixture. All the amplitude-sweep curves have been measured with a solvent trap allocated between both disks during the measurements. The temperature was set constant at 37 °C, and the oscillating shear strain was varied under a linear ramp from 0.1% to 1000% with a constant angular frequency of 1 rad s^{-1} . The measurements were performed in triplicate for several mixtures: (i) Gelatin (7% wt/v) with fibrinogen (4% wt/v). (ii) Gelatin (7% wt/v) with fibrinogen (4% wt/v) and Matrigel (50% v/v). (iii) Gelatin (7% wt/v) with fibrinogen

(4% wt/v) and thrombin (1.67 units ml^{-1}). (iv) Gelatin (7% wt/v) with fibrinogen (4% wt/v), thrombin (1.67 units ml^{-1}), and Matrigel (50% v/v). The obtained data was acquired using the software Anton Paar RheoCompass V1.34.1048 and post-processed and plotted with GraphPad Prism 10. The temperature sweep curves were measured using an Anton Paar rheometer MCR 702, equipped with an upper disk of 40 mm diameter and 1° angle (CP40-1), with a fixed working gap of 0.078 mm. The system was also equipped with a solvent trap allocated between both disks during the measurements. The oscillating shear strain was maintained constant at 1 %, and the angular frequency was also set to 1 rad s^{-1}. We previously ensured that these values were within the linear viscoelastic regime of the analyzed materials. The temperature varied from 4 °C to 50 °C for the mixtures: (i) Gelatin (7% wt/v) with fibrinogen (4% wt/v). (ii) Gelatin (7% wt/v) with fibrinogen (4% wt/v) and thrombin (1.67 units ml^{-1}). (iii) Gelatin (7% wt/v). And from 30 °C to 50 °C for the mixtures: (iv) Gelatin (7% wt/v) with fibrinogen (4% wt/v), thrombin (1.67 units ml^{-1}), and Matrigel (50%v/v). (v) Gelatin (7% wt/v) with fibrinogen (4% wt/v) and Matrigel (50% v/v). All measurements were performed in triplicate, acquiring the data using the software Anton Paar RheoCompass V1.34.1048, and the post-processing and plotting were performed with GraphPad Prism 10.

2.7. Electrical stimulation of 3D bioprinting muscle bioactuators

The 3D bioprinted bioactuators were stimulated with a set of carbon-made electrodes attached to the cover of a Petri dish under an inverted microscope (Leica Thunder) with pulses of 2 ms and 1 V mm^{-1} . Analysis of the contractions was performed using a homemade Python algorithm based on computer vision techniques that computed the distance between frames of a selected ROI by applying an L2 norm to the image pixels.

2.8. Cell viability

Cell viability was analyzed using the dual-fluorescence Live/Dead® Viability/Cytotoxicity kit for mammalian cells (Life Technologies) following the manufacturer's instructions. Fluorescently labeled fibers were imaged under a Leica DMi8 inverted fluorescence microscope equipped with a 37 °C and 5% CO2 chamber using a 20× air objective. The percentage of live and dead cells was calculated using ImageJ software ver.1.47q (National Institutes of Health, Bethesda, MD, USA).

2.9. Immunofluorescence staining

3D-bioprinted constructs were washed twice in PBS and fixed by incubating them with a 3.7% v/v) paraformaldehyde in PBS solution for 60 min at RT, followed by three washes in PBS. For MyoD and Myogening staining, fixed samples were previously cryopreserved and cryosectioned. Firstly, samples were embedded in optimal cutting temperature (OCT) compound (Sigma-Aldrich, P0091-6X120ML) using disposable plastic cryomolds. For cryopreservation, the cryomolds were immersed in isopentane pre-cooled in liquid nitrogen until the OCT solidified, turning opaque white. Samples were then stored at −20 °C until sectioning. Cryosectioning was performed using a Leica CM1900 cryostat, generating 10 μm thick sections, which were mounted on Superfrost Plus™ adhesion slides and stored at −20 °C. For immunofluorescence staining, cells were permeabilized by using 0.2% v/v Triton-X-100 in PBS. After two washes with PBS, the constructs were incubated with 5% wt/v bovine serum albumin (BSA) in PBS (PBS-BSA) to block non-specific binding. Then, samples were incubated over night at 4 °C with the primary antibody, for instance Alexa Fluor®488-conjugated Anti-Myosin 4 antibody (eBioscience, 53-6503-82, dilution 1/400, dark conditions), rabbit anti-Alpha sarcomeric actinin (Abcam, ab137346, 1/200 dilution), rabbit anti-MyoD (Abcam, ab307805, 1/100 dilution) and rabbit anti-Myogenin (Abcam, ab124800, 1/100 dilution) in 5% wt/v PBS-BSA. Excepting the already conjugated Anti-Myosin 4 antibody, an incubation with a secondary antibody (anti-rabbit Alexa Fluor 488, Abcam, ab 15 077, 1/1000 dilution, 2 h, RT, in 5% wt/v PBS-BSA) was needed to visualize the other primary antibodies. It is important to mention that for MyoD and Myogenin visualization, since both primary antibodies were of rabbit origin and the same secondary antibody was used for detection, staining was conducted on separate slides containing tissue sections from the same sample to prevent crosstalk between signals. Them, after PBS washings to remove the unbound antibodies, a PBS solution containing 1 μl ml^{-1} Hoechst 33 342 (Life Technologies) was added for 10 min at RT. Finally, the samples were washed twice with PBS and stored at 4 °C until further analysis. Fluorescently immunostained fiber constructs were imaged under a Zeiss LSM 800 confocal scanning laser microscope, with a diode laser at 488 nm and 405 nm excitation wavelengths for Alpha sarcomeric actinin and Myosin 4, and cell nuclei, respectively. MyoD and Myogenin visualization in cryosectioned samples was performed using a Leica Thunder microscope with 488 nm and 405 nm excitation lasers. The percentage of MyoD- and Myogenin-positive cells was quantified from $N = 4$ images of each staining from conventional and PACA-3D samples using the Cell Counter plugin in ImageJ. To improve visual distinction, the fluorescence signal from the Alexa 488 secondary antibody (originally green) was reassigned to red for MyoD and yellow for Myogenin in ImageJ. The orientation and alignment of the myotubes

were analyzed using ImageJ with plugin directionality. Histograms and angle dispersion values were obtained from the fast Fourier transform (FFT) of the Myosin 4 immunostaining images. Fusion index was also calculated from the same Myosin 4 staining images.

2.10. Force measurement

Evaluation of the force output of muscle tissues was performed as reported by Mestre *et al.* [10] Briefly, a two-post system, where the tissue is directly printed and maintained during differentiation, was used as a force measurement platform. Muscle contraction was induced with pulse electrical stimulation by applying 15 V at a 1 Hz frequency of 2 ms. Contractile tissues generated a force against the flexible posts that bent synchronously with the applied electrical pulse. The recording of the setup was performed using a Thunder Leica microscope, where the bending of the post could be easily tracked. Then, to estimate the force exerted against the post, Euler–Bernoulli's beam bending equation was used, that is, using the following equation:

$$P = \frac{3 \cdot E \cdot Iz \cdot y(a)}{a \hat{} 3}$$

where P is the applied force, E is Young's modulus, Iz is the second moment of area of the post around the z-axis, a is the height from which the tissue is exerting the force, and $y(a)$ is the displacement of the post at this height.

2.11. RNA extraction and real time quantitative PCR (RT-qPCR)

To evaluate the mRNA expression of myogenic markers such as MyoD, myogenin, and MyHCI, the total RNA content from 4 to 6 biological replicates of muscle tissues printed with the PACA-3D and conventional approaches was extracted at days 0, 4, 9, and 12 of differentiation. The RNeasy Mini Kit (Qiagen, 74134) was used for this purpose. RNA was quantified by measuring absorbance at 260 nm in a NanoDrop spectrophotometer (ND-1000, NanoDrop) and converted into cDNA using the ReverAid First Strand cDNA Synthesis Kit (Thermo Scientific™, K1622). Finally, 500 ng of cDNA was mixed with the corresponding forward and reverse primers together with PowerUp SYBR Green Master Mix (Applied Biosystems, A25742), following the manufacturer's instructions, and RT-qPCR was carried out in an Applied Biosystems StepOnePlus Real-Time PCR system (Applied Biosystems, 4376600). The list of primers used can be found in the supplementary information. All genes were normalized to GAPDH expression levels.

3. Results and discussion

3.1. The PACA-3D

The skeletal muscle is composed of bundles of muscle fibers (figure 1(A)), which are the basic contractile units of the muscle and are created after fusion of myoblasts and their precursor cells during the differentiation process [44]. Inside each muscle fiber, groups of internal protein structures, called myofibrils, are formed [45]. Moreover, in the native tissue, each bundle of myotubes is further organized in the fascia or fascicles surrounded by the perimysium, a layer of connective tissue (mainly collagen) that stabilizes and separates the bundles of muscle fibers, containing 10–100 bundles [46]. In this study, we aimed to replicate this complex hierarchical structure using PACA-3D.

Co-axial 3D bioprinting is a method that allows printing of cell-laden hydrogels surrounded by a shell of another hydrogel, usually assisting the crosslinking of the inner hydrogel. One of the most common strategies for co-axial printing is the use of alginate, which is crosslinked *in situ* during the extrusion process in the presence of calcium chloride in the outer needle. However, this method can be difficult to regulate, as the calcium chloride flow in the solution is difficult to control (requiring the use of syringe pumps to achieve sufficiently small and controlled flows) and the obstruction of the internal nozzle often occurs due to the accumulation of crosslinked alginate [47].

To overcome these difficulties, we considered an alternative approach based on using a sacrificial material as a supporting structure during the 3D bioprinting process. To this end, we chose the block co-polymer pluronic acid F-127, which has been successfully used as a sacrificial ink for structures that need infilling or three-dimensional support before crosslinking [48]. However, pluronic acid has never been implemented in a co-axial system to act as a shell to finely tune the thickness of the hydrogel extruded in the inner needle.

Figure 1(B) shows a comparative schematic of the working principles of conventional 3D bioprinting and our pluronic-assisted co-axial 3D bioprinting method. The key difference lies in the fact that, in conventional printing, a single syringe containing the cell-laden bioink is extruded alone, layer by layer, without the use of any physical confinement. Crosslinking can be achieved through chemical, temperature or light-induced crosslinking, usually after the bioprinting, although some choose to perform crosslinking during the extrusion process [19, 20]. In contrast, we present as an alternative approach PACA-3D printing to produce highly fiber-controlled and independent filaments. This involves the co-extrusion of the inner bioink with a sacrificial material in the outer layer (movie S1 and

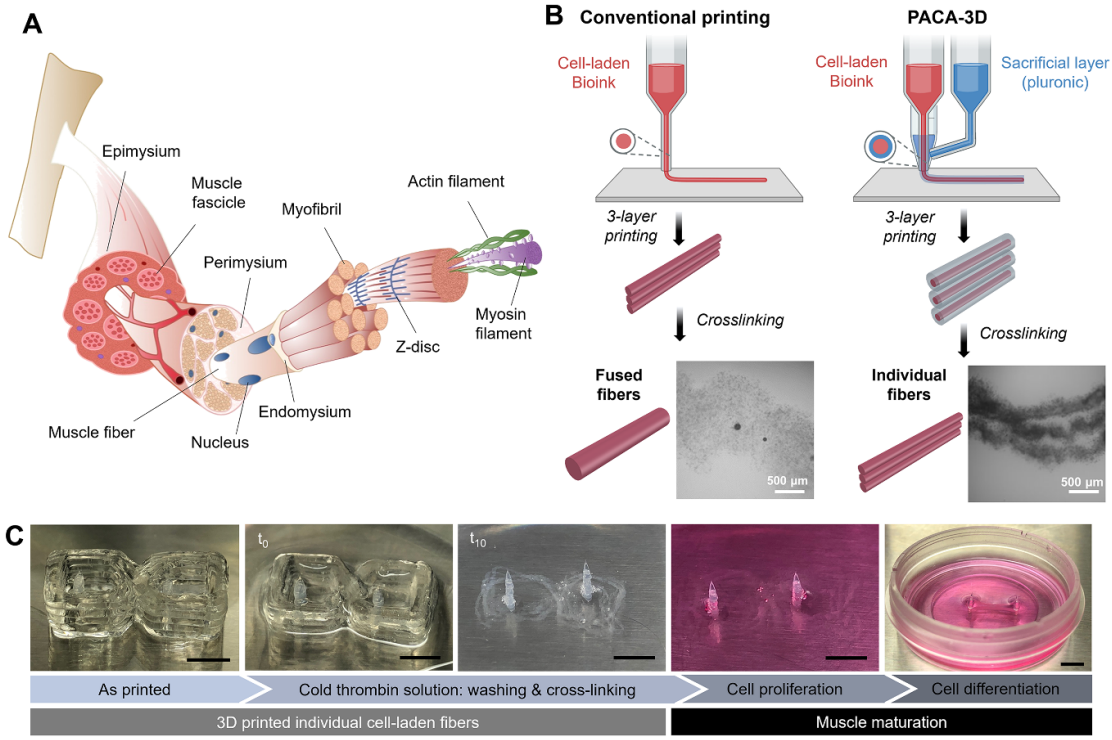

Figure 1. Fabrication of bundle-like structures using pluronic-assisted co-axial 3D bioprinting technique (PACA-3D). (A) 3D structure of the skeletal muscle tissue hierarchically organized in fascicles, containing several bundles of multinucleated myofibers. (B) Schematics of conventional and pluronic-assisted coaxial 3D bioprinting. In conventional bioprinting, the layers fuse together during the crosslinking process, resulting in a single filament. In coaxial bioprinting, bioink layers do not fuse due to the co-extrusion with pluronic acid (sacrificial material). Therefore, after bioink crosslinking and washing of the pluronic, thinner individual filaments are obtained. (C) The printed construct is washed and crosslinked simultaneously to finally obtain individual thin filaments (images at time 0 min and 10 min, respectively). Later, printed tissue is maintained in GM for two days and then changed to DM to induce differentiation into myotubes in the two-post system. Scale bar: 5 mm. Created in BioRender. Sánchez (2025) https://BioRender.com/2h2rg40.

figure S1). Specifically, in this approach, pluronic was used to provide a confinement layer during printing, maintaining the fiber structure until crosslinking. Pluronic undergoes a sol–gel transition at room temperature, going from liquid below ∼ 4 °C to a gel at room temperature, making it ideal for 3D printing and obtaining fine control of its extrusion. Compared to conventional printing, with PACA-3D bioprinting, thin, individual, width-controlled filaments that do not fuse with each other can be printed. With this method, there is no need to crosslink the hydrogel during extrusion, but simple physical confinement between the cell-laden hydrogel and pluronic ensures the confinement of the hydrogel.

Both strategies provide initial stability of the 3D-bioprinted filaments and allow for second-level and final crosslinking by any available approach, namely: (i) UV-crosslinking, (ii) temperature-assisted crosslinking, (iii) enzymatic crosslinking, or (iv) ionic crosslinking. Once the cell-laden hydrogel is crosslinked, pluronic can be removed by the addition of cold PBS, inducing its dissolution at low temperatures. As an example, figure 1(C) shows the process of a cell-laden hydrogel composed of gelatin and fibrinogen with C2C12 cells. The physical contact between gelatin and pluronic in their gel form helps the filaments to retain their shape and not fuse with each other until crosslinking. Crosslinking of fibrinogen-based hydrogels is triggered by the addition of thrombin, which is already mixed in the cold PBS solution, both dissolving the pluronic outer shell and crosslinking the fibrinogen within the cell-laden hydrogel at once. As shown in figure 1(C), the muscle constructs were directly bioprinted and maintained in a two-post system (flexible PDMS-based pillars) during the muscle maturation process. This setup, which has been previously reported [10], not only provides mechanical stability and constant tension to the printed muscle, which contributes to improved cell differentiation and muscular fiber alignment, but also serves as a platform to measure the contractile force.

The printing fidelity of a hydrogel is highly dependent on the type of nozzle and its gauge. Conical nozzles, which are usually fabricated in plastic, provide better stress profiles for 3D bioprinting because the point of maximum stress is only found at the end of the tip. In contrast, cylindrical nozzles made of stainless steel could be potentially harmful to cells as the shear stress increases

significantly when they are too long. Previous reports on co-axial or core–shell printing have used cylindrical needles as they are easier to assemble [47, 49, 50]. Here, however, we looked for a strategy that could include conical needles in the co-axial design, causing less damage to cells (detailed information about the optimization of the co-axial needles can be found in SI, figure S2).

3.2. The confinement methods and materials

Using pluronic acid as a sacrificial material offers high versatility to implement several crosslinking strategies, not restricting its use to skeletal muscle cells but potentially amplifying its use for many kinds of tissues that might require different hydrogel compositions. Based on these properties, two different hydrogel confinement strategies were envisaged: (i) a chemical method, based on the *in-situ* crosslinking of alginate inside the hydrogel with $CaCl_2$ present in the pluronic solution, and (ii) a physical method, based only on physical repulsion by gelatin inside the hydrogel and pluronic outside of it, as previously mentioned (figure 2(A)).

Both chemical and physical confinement methods allow for a great degree of flexibility in the choice of materials. The chemical confinement method is ideal for materials that require ionic crosslinking, such as alginate, as these ions can be dissolved at the desired molarity in pluronic at low temperatures, whereas the uncrosslinked material is added as part of the cell-laden hydrogel. Alginate and calcium chloride, one of the most widely used pairs, are a great choice for this method; however, in principle, any other similar combination of materials could be used (i.e. gellam gum and chitosan). Alginate crosslinks rapidly when it reacts with calcium ions, often leading to the obstruction of the internal nozzle due to the accumulation of crosslinked alginate. In our strategy, when calcium chloride is dissolved in a pluronic solution, it creates a more viscous medium, which slows the diffusion of calcium ions toward the alginate in the inner layer. This slower diffusion rate could result in a more controlled and gradual crosslinking process of alginate while being extruded from the nozzle, reducing clogging. For instance, in our implementation, Ca^{+2} ions from pluronic are in contact with alginate at the borders of the filament, chemically crosslinking it to achieve a homogeneous filament. The physical method, on the other hand, only requires the cell-laden hydrogel to be in a gel form at the bioprinting temperature. Gelatin, as we already showed, is an adequate choice for this method, as it is cheap, biocompatible, and widely used in 3D bioprinting due to its shear-thinning behavior and because it can be washed away during incubation. As with the chemical confinement method, any other material with similar gel properties can be used instead (i.e. GelMA). However, gelatin is particularly advantageous as it can be mixed with other hydrogels that are more liquid, such as fibrinogen, collagen, Matrigel, or alginate, serving as a supporting hydrogel to obtain very thin filaments, which is difficult to achieve with low-viscosity hydrogels. It is important to highlight that the gelatin used in this study is not crosslinked, as it is just used as a viscosity modulator to both allow printing fidelity and maintain the structural shape of the 3D printed construct until the other components (e.g. fibrinogen) are crosslinked.

The versatility to adapt PACA-3D to different confinement schemes and crosslinking methods leads to a great variety of combinations of materials depending on the specific requirements of cell lines, potentially covering a wide area of applications. Table 1 shows a qualitative overview of some of the most used materials in 3D bioprinting that can be implemented in both strategies, such as GelMA, fibrinogen, and collagen or Matrigel. The column filament quality reports in a qualitative manner homogeneity of the printing and the stability of the filaments. This is reported in qualitative terms, as it is not possible to report absolute values of pressure, as they highly depend on the bioprinter, microfluidics tubing, and other system parameters, and should therefore be optimized by each user. For instance, physical confinement of a hydrogel only containing Matrigel, or collagen type I might give homogeneous filaments if the concentration of gelatin is high enough (i.e. at least 3% wt/v), but their stability is low, as their stiffness of the construct after temperature crosslinking is low. Therefore, thin and homogeneous filaments can be printed with this combination, but they are easily broken. Adding fibrinogen to the mixture increases their long-term stability, as fibrin is more robust, creating high quality filaments. A similar effect occurs with the chemical confinement method. If the main biomaterial is too liquid, like Matrigel, it will diffuse through the pluronic before the Ca-crosslinking of alginate can form homogeneous filaments, unless the concentration of alginate is increased to accelerate this process. Since alginate does not have cell attachment motives, it is advisable to keep its concentration as low as possible; in that case, however, the quality of the filaments will not be high. One of the best strategies to follow is the combination of both methods by adding a small amount of gelatin or GelMA to alginate, using a hybrid chemical-physical method of confinement. With this combination, as can be seen in the table, the quality of the filaments is much improved and virtually any material can be used with it.

Collagen and Matrigel, which are crosslinked slowly at 37 °C for approximately 30 min in an irreversible manner, deserve special consideration. Collagen type I is one of the main components of many tissue's ECM and, in particular, of skeletal muscle tissue, making it especially interesting for 3D bioengineering applications [51]. Also, Matrigel is

Table 1. Relation of different strategies to obtain thin, independent filaments, combining different biomaterials, confinement strategies and crosslinking methods.

Type of confinement	Confinement material (outer nozzle)	Gelation temperature of confinement material	Bioink (inner nozzle)	Crosslinking	Filament quality
Physical	Pluronic	Gelation: 37 ° CS-G transition: 4 °C	Gelatin Collagen	— Temperature (37 °C)	Low
Physical	Pluronic	Gelation: 37 °C S-G transition: 4 °C	Gelatin Matrigel	— Temperature (37 °C)	Low
Physical	Pluronic	Gelation: 37 °C S-G transition: 4 °C	Gelatin Fibrinogen	— Enzymatic (Thrombin)	High
Physical	Pluronic	Gelation: 37 °C S-G transition: 4 °C	Gelatin Fibrinogen Matrigel	— Enzymatic (Thrombin) Temperature (37 °C)	High
Chemical	Pluronic + $CaCl_2$	Gelation: 25 °C S-G transition: 4 °C	Alginate Matrigel	Chemical ($CaCl_2$) Temperature (37 °C)	Medium
Physical and chemical	Pluronic + $CaCl_2$	Gelation: 25 °C S-G transition: 4 °C	Gelatin Alginate Matrigel	— Chemical ($CaCl_2$) Temperature (37 °C)	High
Physical and Chemical	Pluronic + $CaCl_2$	Gelation: 25 °C S-G transition: 4 °C	Gelatin Alginate Fibrinogen	— Chemical ($CaCl_2$) Enzymatic (Thrombin)	High
Physical and chemical	Pluronic + $CaCl_2$	Gelation: 25 °C S-G transition: 4 °C	Gelatin Alginate Fibrinogen Matrigel	— Chemical ($CaCl_2$) Enzymatic (Thrombin) Temperature (37 °C)	High
Physical and chemical	Pluronic + $CaCl_2$	Gelation: 25 °C S-G transition: 4 °C	GelMA Alginate Fibrinogen	UV-light Chemical ($CaCl_2$) Enzymatic (Thrombin)	High
Physical and chemical	Pluronic + $CaCl_2$	Gelation: 25 °C S-G transition: 4 °C	GelMA Alginate Fibrinogen Matrigel	UV-light Chemical ($CaCl_2$) Enzymatic (Thrombin) Temperature (37 °C)	High

one of the most widely used basement membrane matrices for 2D and 3D cultures, since it is rich in collagen and many other ECM proteins, but shares the same difficulties. However, their irreversible and low temperature-dependent crosslinking makes difficult their bioprinting, as opposed to gelatin, which has reversible crosslinking. Both materials are liquid at room temperature and cannot be 3D-bioprinted by pneumatic extrusion, but if they are crosslinked at 37 °C, they are also too stiff to be extruded. Although the most promising approaches in the literature have dealt with the mixture of alginate and collagen to achieve proper extrusion [52], better strategies are necessary in the field. One of the main difficulties with these approaches comes from the slow crosslinking of these materials. Because of this, the printed construct can easily lose its shape before the crosslinking has taken place. For that reason, collagen or Matrigel have been mainly used with casting molds, which can retain the shape of the construct until the hydrogel is fully crosslinked [53]. With the pluronic-assisted co-axial printing method, however, these materials can be protected during crosslinking at 37 °C, avoiding its diffusion in the medium,. As pluronic does not dissolve at this temperature, the filaments can be incubated in physiological temperatures for 30–45 min until Matrigel or collagen have been crosslinked, and then pluronic can be removed with cold PBS. Both confinement methods (either chemical or physical) could potentially be used in combination with this type of hydrogel, followed a tertiary crosslinking with fibrinogen to improve the mechanical stability of the filaments.

The summary presented in table 1 is a fast guide for understanding the possible material combinations according to their confinement method; however, the reality is much more complex. The relative concentrations of the confinement materials, as well as those of pluronic and even $CaCl_2$, greatly influence the applicability of the co-axial printing method, as depicted

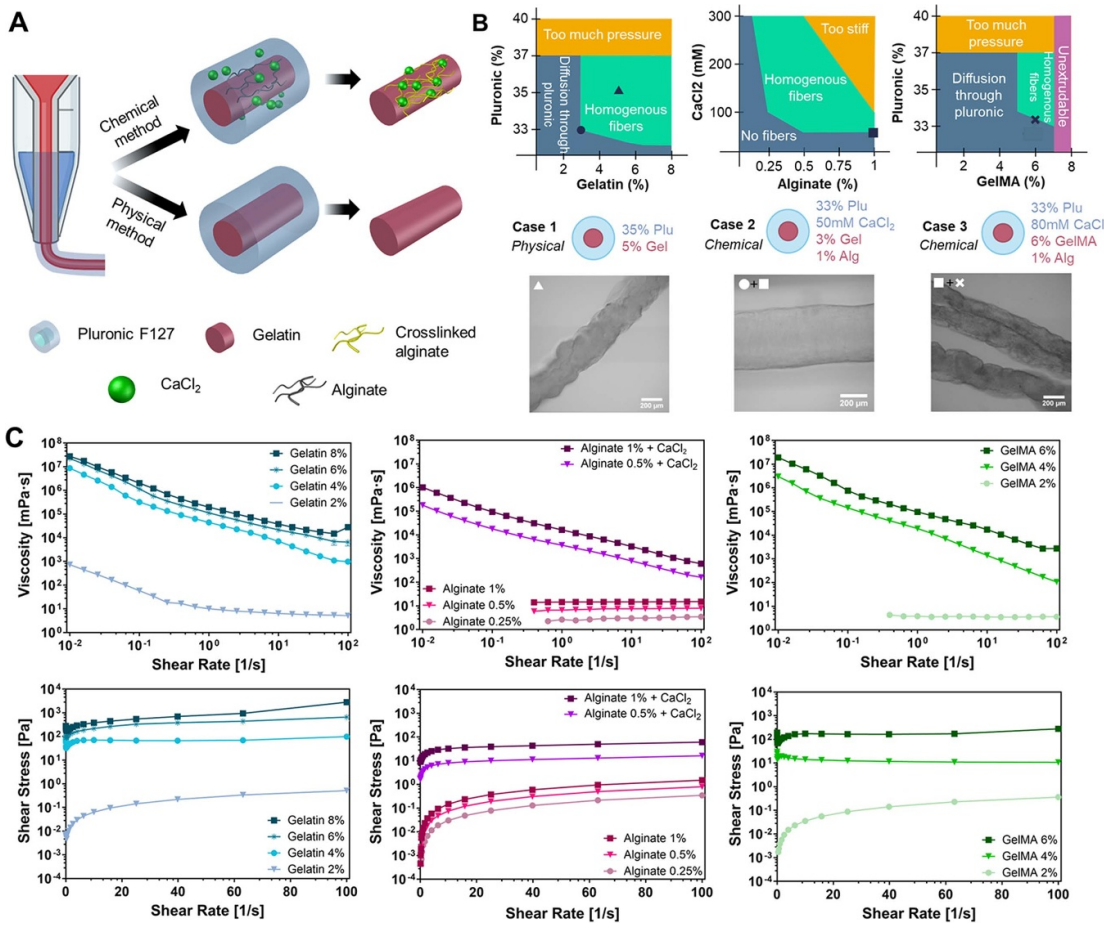

Figure 2. PACA-3D printing and rheological characterization of different biomaterials commonly used tissue bioengineering. (A) Schematic representation of the two different confinement methods (chemical and physical) used for co-axial bioprinting. This figure has been created with BioRender.com. (B) Ranges of application of different materials according to their confinement method. Each symbol represents a specific hydrogel composition. The case numbers are examples of bioinks with different combinations of hydrogel compositions. (C) Rheological characterization (viscosity curves) of materials at different concentrations commonly used in tissue engineering. Created in BioRender. Sánchez (2025) https://BioRender.com/s8uski1.

in figure 2(B). Regarding the physical confinement method, the concentration of gelatin with respect to the concentration of pluronic must be adjusted to avoid bioink diffusion in the outer shell. In general, gelatin at concentrations below 3% (wt/v) is liquid enough to diffuse through pluronic. At the same time, pluronic at concentrations below 33% (wt/v) is not viscous enough to prevent bio-ink diffusion. Therefore, the ideal range of concentrations for gelatin to obtain homogeneous filaments, as the one shown in case 1, is between 3%–8% (wt/v); for pluronic, it is between 33%–37% (wt/v). Higher concentrations of pluronic and gelatin could still be successfully used. However, they might require a pressure range that is too high for 3D bioprinters (depending on the specific bioprinter model), and cells might suffer excessive shear stress during extrusion. The chemically assisted method, based on alginate crosslinking during extrusion, provides improved filament homogeneity compared to physical confinement, as shown in figure 2(B). Moreover, it does not present clogging problems since the flow of pluronic can be carefully controlled by the applied pressure. Alginate concentrations ranging from as low as 0.25% (wt/v) can yield to homogeneous filaments if the concentration of $CaCl_2$ is high, and other materials that increase the viscosity are present in the mixture. Higher concentrations of alginate, even surpassing 1% (wt/v) can, naturally produce very homogeneous filaments, but its stiffness might be too high for the cells, considering that other biocompatible polymers with attachment sites, like fibrinogen or collagen, should be included in the mixture. If needed, alginate can be removed after crosslinking the main biomaterial by adding ethylenediaminetetraacetic acid EDTA for 5 min [49, 54].

Finally, another possible strategy consists of a hybrid chemical-physical confinement method that uses both gelatin and alginate in smaller quantities. Case 2 in figure 2(B) shows an example of this, where alginate at 1% (wt/v) was ionically crosslinked with 50 mM of $CaCl_2$ (square symbol), with gelatin at 3% (wt/v) as extra support (circular symbol). Notice how the filament is much more homogeneous than case 1, in which 5% (wt/v) of gelatin was used

(triangular symbol). Therefore, decreasing the gelatin concentration, together with the addition of alginate, resulted in a smoother filament shape. GelMA can also be used to achieve physical confinement, as it also exhibits gel properties. However, gelatine and GelMA gelification are slightly different due to the methacrylation process occurring during GelMA synthesis [55]. This can be seen in the relationship between the pluronic and GelMA concentrations. GelMA gelates at higher concentrations than gelatin, requiring a minimum concentration of 5% (wt/v) compared to the minimum of 3% (wt/v) for gelatin (figure 2(B)). Regarding GelMA, the optimal concentration range for obtaining homogeneous filaments was 5%–7% (wt/v). For concentrations higher than 7% (wt/v), the mixture was completely unextrudable. It should be noted that in case of gelatin, the printable concentration range is from 3%–8% (wt/v) being broader than GelMA. Homogeneous filaments were also obtained when alginate was added to the mixture, as shown in case 3 (square and cross sympols).

Figure 2(C) shows the rheological properties of hydrogels composed of gelatin, GelMA, and alginate at different concentrations. Viscosity curves of gelatin and GelMA indicate the non-Newtonian behavior of these materials at a concentration above the 2% (wt/v), as shown by the decrease in viscosity when higher shear rates are applied. Indeed, this behavior corresponds to shear thinning materials, which are commonly used in extrusion-based 3D printing to allow the printing of homogeneous filaments. Interestingly, both gelatin and GelMA at 2% (wt/v), although GelMA specially, do not exhibit non-Newtonian properties, as the viscosity remains mostly constant when increasing the shear rate, meaning that at low concentrations, the hydrogel is mostly liquid and therefore not suitable for extrusion printing. Similar results were observed for alginate. Alginate at the concentrations reported in this study show Newtonian properties (i.e. viscosity is constant regardless of the shear rate), but when calcium chloride is added to the solution to induce alginate crosslinking, the final hydrogel presents a shear thinning behavior similar to gelatin and GelMA.

3.3. Biofabrication and characterization of skeletal muscle bioactuators with fascicle-like structures using PACA-3D

3.3.1. Rheological characterization of bioinks for skeletal muscle fabrication

Fibrinogen has been extensively used for skeletal muscle tissue bioengineering, either alone or in combination with others, such as Matrigel, collagen, and/or gelatin [3, 53]. Supplementary figure S3 shows the range of applications of some of these mixtures, focusing on their concentrations as a function of the attachment sites that they provide and the density of the matrix. The relative combination of these materials must be carefully considered, as the resulting bioink must be extrudable, homogeneously mixed, and after crosslinking, the matrix must not be too dense for cell proliferation. For instance, gelatin was included in all bioinks, as it provided the required viscosity for extrusion. When combining fibrinogen with gelatin, the ideal ratio should be maintained between 3 and 8% (wt/v) of gelatin and 1% and 4% of fibrinogen to obtain a bioink with proper density and sufficient attachment sites (cases 1 and 2). If Matrigel is mixed at a 30% (v/v) concentration with gelatin 7% (wt/v), we suggest decreasing fibrinogen to a range as low as 1%(wt/v) (Case 3). However, if fibrinogen concentration is too low, the density of attachment sites of Matrigel and its stiffness are not high enough for proper cell differentiation, as case 4 shows (50% (v/v) Matrigel, gelatin 7% (wt/v), and no fibrinogen). Matrigel and gelatin present a liquid consistency at 4 °C and 37 °C, respectively. This poses a challenge when both materials are mixed as the crosslinking temperature of Matrigel is 37 °C. Therefore, a mixture of these two materials can lead to a non-homogeneous bioink.

The rheological properties of these biomaterials haven been assessed in order to further evaluate their printability. Figure 3(A) shows the viscosity and flow curves of a hydrogel mix composed of 4% (wt/v) fibrinogen and gelatin at different concentrations ranging from 2%–8% (wt/v). When comparing these graphs with the ones obtained from gelatin hydrogels (figure 2(C)), no significant differences in viscosity when gelatin was at 4%, 6%, or 8% (wt/v) were observed. However, at 2% (wt/v) of gelatin, we observed an increase in viscosity when the fibrinogen was added to the solution, indicating that fibrinogen improves the printability of hydrogels at low gelatin concentration range (note that thrombin is added after the extrusion process, so it is not relevant to study its effect at this stage). Moreover, the shear moduli of gelatin- and fibrinogen-based hydrogels with and without Matrigel over time were evaluated. The graph in figure 3(B) shows the transition from the liquid to the gel state when fibrinogen was added to the mixture, simulating the state after the bioprinting process. The chemical crosslinking of fibrinogen with thrombin and the thermal crosslinking of Matrigel and gelatin induced an increase in the storage modulus over the loss modulus over time. When Matrigel was added to the hydrogel mix, there was a faster transition to gel, as indicated by a storage modulus higher than the loss modulus acquired during all the measurement times. This could present difficulties in terms of bioprinting, as irreversible gelation of Matrigel could lead to partial or complete blockage of the syringe. These results suggest that the gelatin-fibrinogen mix is the optimal hydrogel for cell proliferation, due to its rheological behavior during the printing process and reversible gelation, both associated with gelatin presence and the

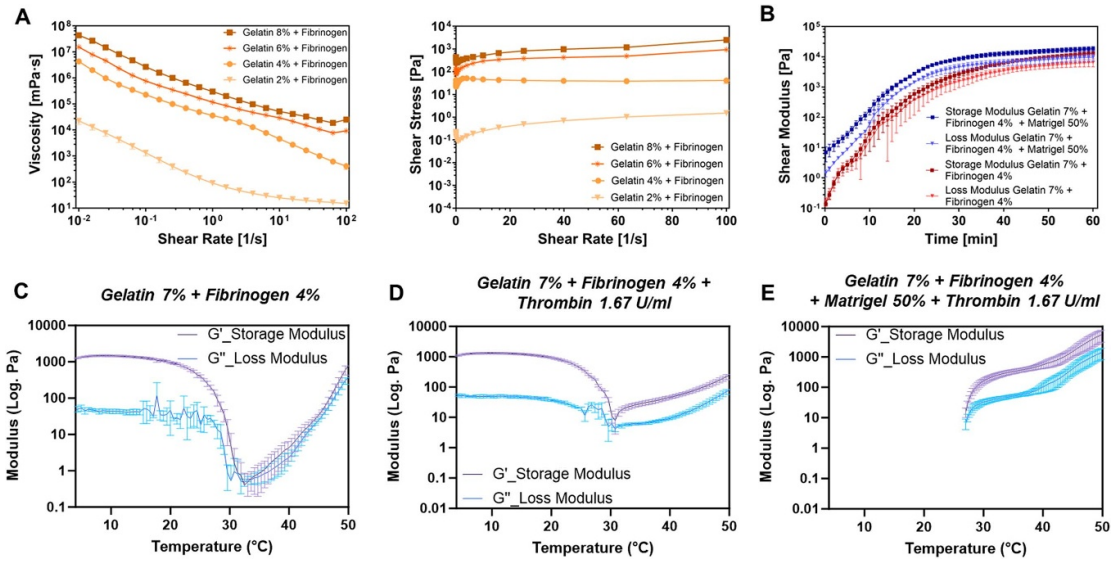

Figure 3. Rheological characterization of bioinks for 3D bioprinting of skeletal muscle bioactuators. (A) Viscosity curves (right) and flow curves (left) of gelatin-fibrinogen hydrogels at different gelatin concentrations, with fibrinogen fixed at 4% (wt/v). (B) Evolution of shear modulus of gelatin-fibrinogen hydrogels with and without Matrigel over time, starting from the point at which thrombin is added to the mixture, which is kept at 37 °C to induce Matrigel crosslinking as well. (C)–(E) Temperature sweep measurements performed at an oscillating shear strain of 1% and an angular frequency of 1 rad s^{-1} . (C) Gelatin 7% with Fibrinogen 4 %. (D) Gelatin 7% with Fibrinogen 4% and Thrombin 1.67 units ml^{-1}. (E) Gelatin 7% with fibrinogen 4 %, Thrombin 1.67 units ml^{-1} and Matrigel 50 %.

abundance of cell attachment sites attributed to fibrinogen. Therefore, a combination of 7% (wt/v) of gelatin and 4% (wt/v) of fibrinogen was used for the 3D bioprinting of skeletal muscle tissues, as will be described in the next sections. Nevertheless, it remained necessary to further assess the effects of fibrinogen, Matrigel, and thrombin on the rheological properties of gelatin by performing amplitude sweep measurements at a constant temperature of 37 °C, with a linear ramp from 0.1% to 1000% shear strain and using a solvent trap to decrease the dehydration of the materials (figures 3(C)–(E) and S4). For a 7% (wt/v) gelatin solution mixed with 4% (wt/v) fibrinogen (figure S4(A)), we observed a breaking point at 6.3% shear strain, where *G*' and *G*" intersected, indicating a transition from elastic to viscous behavior. Prior to this point (0.1%–6.3% shear strain), *G*' remained higher than *G*", signifying the material's predominantly elastic nature. However, both moduli were notably low, reaching only 0.14 Pa at the breaking point. The addition of 50% Matrigel to the gelatin/fibrinogen mixture (figure S4(B)) significantly altered the material's mechanical response. We observed constant values for both the storage (*G*') and loss (*G*") moduli up to approximately 20% shear strain, with the breaking point shifting to ∼62% shear strain. This shift, along with a slight increase in modulus values, suggests that Matrigel reinforces the hydrogel structure, likely through physical interactions that create additional crosslinks within the polymeric network, which is in line with reported works [56]. The most significant improvement in hydrogel stability was observed upon introducing a chemical crosslinker. The addition of 1.67 units ml^{-1} thrombin, which enzymatically crosslinks fibrinogen, resulted in the complete absence of a breaking point across the entire strain range (figure S4(C)). Since *G*' remained greater than *G*" throughout the shear strain ramp, we conclude that fibrinogen, when chemically crosslinked, provides substantial reinforcement to the hydrogel, maintaining its integrity even under high strain conditions (>100 %). A similar stabilization effect was observed when both Matrigel and thrombin were added to the system (figure S4(D)). This further emphasizes that chemical crosslinking is significantly stronger than physical interactions. Ultimately, these results demonstrate that thrombin-mediated crosslinking is the primary factor enhancing the hydrogel's mechanical strength at 37 °C. Based on this analysis, we selected 1% shear strain as a representative value within the linear viscoelastic regime for temperature ramp analysis, using 1% shear strain and an angular frequency of 1 rad s^{-1}.

We assessed the thermoresponsive behavior of 7% (wt/v) gelatin by evaluating the evolution of its rheological moduli over a temperature range of 4 °C–50 °C. As previously reported, gelatin exhibits highly elastic properties at low temperatures [57]. In figure S5(A), we observed that *G*' remained higher than *G*" between 4 and 31 °C, indicating a predominantly solid-like behavior. However, within the final 5 °C of this range, the material underwent a compositional transition, gradually losing its elasticity. During this phase, *G*'—which was initially above 1000 Pa—decreased significantly until it reached values comparable to *G*". A sharp reduction in the

storage modulus, coupled with its overlap with the loss modulus in the range of 31 °C–50 °C, indicates a shift from an elastic to a more viscous, liquid-like state. A similar trend was observed when gelatin (7% wt/v) was mixed with fibrinogen (4% wt/v), with a clear transition from an elastic to a viscous state occurring around 31 °C (figure 3(C)). However, beyond this temperature, both moduli began to increase again, reaching values as high as 1000 Pa. Despite this increase, *G*' and *G*" remained overlapped, indicating that the material retained predominantly viscous, liquid-like characteristics. This was further confirmed by the complete liquefaction of the solution upon removal of the rheometer disks after measurement (figure S5(B)). We attribute these findings to physical interactions induced by fibrinogen—which likely facilitates physical crosslinking within the gelatin network and thrombin, as reported [58], being this interaction sensitive to temperature—as well as to a slight dehydration process, despite employing a solvent trap throughout all measurements.

We also investigated the effect of the chemical crosslinker thrombin on the thermal stability of the mixture. To do so, we prepared a solution of gelatin (7%) with fibrinogen (4%) and thrombin (1.67 units ml^{-1}) and initiated measurements immediately after adding the crosslinker (figure 3(D)). As shown in the figure, we observed a drop in the moduli around 31 °C, corresponding to the elastic-viscous transition of gelatin. However, unlike previous cases, both moduli did not overlap, indicating that thrombin reinforces the hydrogel structure across the entire temperature range. In other words, the chemical crosslinking ensures that the hydrogel retains its elastic properties, increasing its stiffness.

Finally, we evaluated the complete formulation by incorporating Matrigel (50% v/v) into the hydrogel mixture to assess its overall impact. Initially, we prepared the mixture without thrombin (figure S5(D)). Due to Matrigel's tendency to freeze at low temperatures, measurements were conducted only from 30 °C to 50 °C. The results clearly indicate that Matrigel reinforces the hydrogel structure, as evidenced by *G*' remaining consistently higher than *G*" throughout the temperature range. Notably, the storage modulus remained relatively constant, ranging from 40.8 ± 45 Pa to 93.4 ± 125 Pa, demonstrating that the high concentration of Matrigel contributes a significant elastic component to the mixture. Subsequently, when thrombin was added (figure 3(E)), a similar pattern was observed; however, the chemical crosslinker further enhanced both moduli. At physiological temperature (37 °C), the storage modulus increased to 410.2 ± 108.6 Pa and the loss modulus to 64.1 ± 15.9 Pa. At 50 °C, both moduli exceeded 5000 Pa, demonstrating the combined reinforcing effect of Matrigel and thrombin in enhancing the stiffness of the hydrogel.

3.3.2. Characterization of 3D printed individual filaments with controlled width

One of the most straightforward applications of the PACA-3D technique is found in the 3D bioprinting of skeletal muscle cells, which can benefit the most from the fibrillar structure, inducing self-organization in a fascicle-like manner, as in native tissue.

With any of the two confinement methods mentioned in the previous section, the filament width could be carefully controlled to the desired dimensions by simply modifying the pressure applied during the extrusion process. The desired width is 200 μm for presenting the oxygen diffusion limit within a tissue, being crucial to work within that width values to improve cell viability and therefore, cell differentiation and muscle maturation. Figure 4(A) shows the width range for each case using a bioink formulation consisting of 7% gelatin (wt/v) and 4% fibrinogen (wt/v) for both conventional and physical confinements (using 33% (wt/v) pluronic acid), with the addition of 0.5% (wt/v) alginate specifically for the chemical confinement method (using 33% (wt/v) pluronic acid with 300 mM of $CaCl_2$). For the chemical confinement method, the control was finer than for the physical method, achieving diameters as low as the nozzle diameter (200 μm) for 60 kPa of pressure. However, no continuous filaments were obtained when a pressure of less than 60 kPa was applied. The physical confinement method, on the other hand, could span a width of approximately 200 μm when 50 kPa was applied, to 330 μm when applying 80 kPa—meaning that thinner filaments could be obtained at any working pressure. In any case, the variability was low, as demonstrated by the error bars, indicating that the printed filaments were homogenous. Notice, however, that the exact range of pressure is highly dependent on the characteristics of the bioprinter, tubes, nozzles, and pressure pumps, as well as the hydrogel concentration. Despite the applied pressure range, our method showed great flexibility and homogeneity during bioprinting. Contrary, when using conventional 3D bioprinting, the diameter of the printed filaments was more than double that obtained with co-axial printing, even at low pressures, demonstrating the effectiveness of the PACA-3D printing strategy for fabricating filaments with controlled widths.

Another key advantage of our technology is the fabrication of individual filaments that do not fuse together during crosslinking due to the physical confinement provided by pluronic acid during the extrusion process (figures 4(B)–(I)). This enabled the fabrication of skeletal muscle tissues with fascicle-like structures that resemble native tissues, as shown in figure S6. Although a certain degree of filament fusion took place during the 9 d of muscle cell differentiation, both for PACA-3D and conventional printed filaments (figures 4(B-ii)), it is important to note that

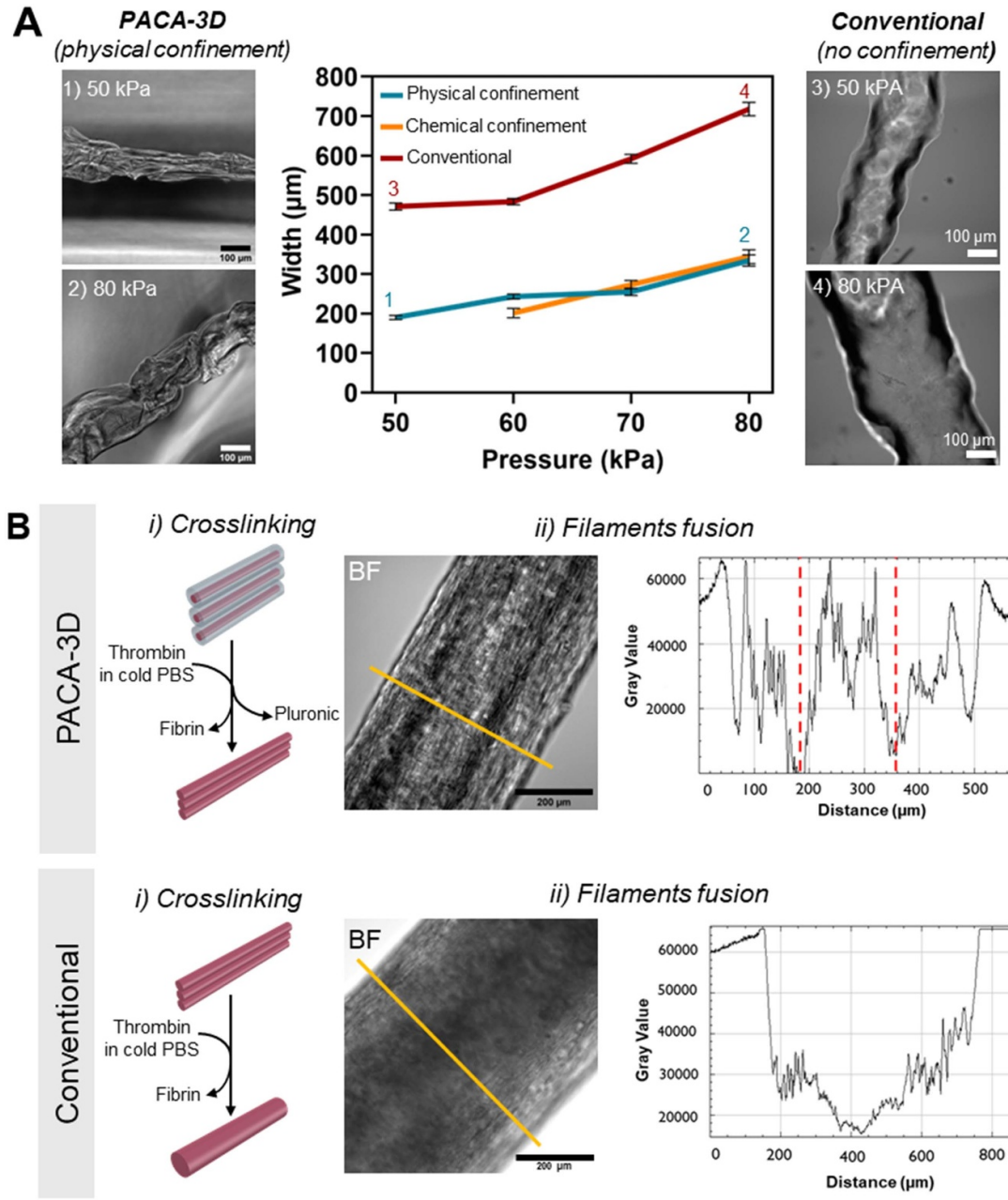

Figure 4. Characterization of the gelatin- and fibrinogen-based bioink for 3D bioprinting of skeletal muscle cells. (A) The filament diameter of a hydrogel composed of gelatin 7% (wt/v) and fibrinogen (4% wt/v) can be carefully controlled by modifying the extrusion pressure during 3D printing. In the case of the chemical confinement, 0.5% wt/v was added to the bioink and 300 mM of $CaCl_2$ was added to the pluronic solution (33% wt/v). Error bars represent standard error of the mean. The bright-field microscopy images correspond to filaments printed under the specified extrusion pressures: Images 1 and 3 were obtained at 50 kPa using physical confinement (PACA-3D) and no physical confinement (conventional printing), respectively, while Images 2 and 4 were obtained at 80 kPa under the same conditions (physical confinement for PACA-3D and no confinement for conventional printing).(B-i) Schematic of the enzymatic crosslinking process of the cell-laden bioink composed of $5x10^6$ ml^{-1} of C2C12 myoblasts, 7% (wt/v) gelatin and 4% (wt/v) fibrinogen with thrombin after 3D bioprinting. Regarding PACA-3D (top), the cold thrombin solution crosslinks the fibrinogen while pluronic acid is being dissolved, resulting in thin individual filaments. (B-ii) Bright field (BF) microscopy images of a skeletal muscle bioactuator fabricated with PACA-3D (top), where 3 layers can be distinguished, and conventional bioprinting (down) where no individual filaments can be observed. On the right, the intensity projection graphs of the microscope images (yellow section).

the key difference is that in conventional bioprinting, such fusion events occur during the crosslinking process, leading to a homogeneous fusion within the filament, resulting in a single construct. In PACA-3D printing, fusion occurs later during the cell differentiation stage, most likely due to ECM remodeling by healthy cells. Indeed, a closer examination of the intensity profile of images acquired by both fabrication techniques shows significant differences between filaments. The intensity profile of the PACA-3D printed filaments showed hills and valleys, consistent with a non-homogeneous hydrogel density, whereas the

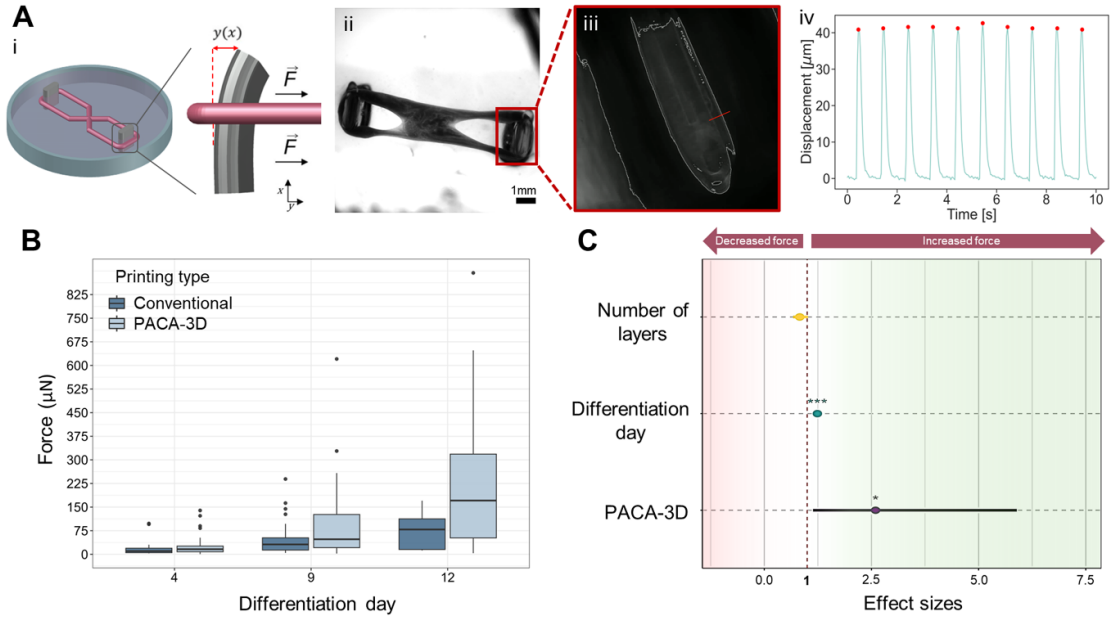

Figure 5. Characterization of the force contraction of the bioactuators. (A) Force monitoring mechanism schematic depicting the evaluation of force output from the 3D-bioengineered skeletal muscle actuators under electrical pulse stimulation (EPS). (A-i) Muscle actuator assembled on force measurement platform. (A-ii) Videos from the contracting muscle are taken, then analyzed via Python. (A-iii) Post silhouette is marked in white, and a perpendicular red line is created to determine the post displacement generating a graph (A-iv) that shows the single-twitch contractions. (B) Force output from muscle-based actuators fabricated using PACA-3D and conventional 3D bioprinting techniques, at day 4, 9 and 12 of differentiation. (C) Mixed effect model on the force output depending on different variables. Variables with effect sizes below 1 have negative impact on the force (red area). Contrary, effect sizes above 1 indicate that the variable presents a positive effect on the force output (green area).

conventionally printed filaments showed a single valley, indicating a single fused filament with homogeneous crosslinking. This effect is also clearly visible in immunostained cryosections in figures 7 and S8, which we will discuss later. We hypothesize that, despite this later fusion, individually printed filaments retain some of their individuality with points of lower density, potentially improving nutrient diffusion to the cells. Certainly, PACA-3D shows greater viability compared to conventional bioprinting, as depicted in figure S2(C) for 3D bioprinting of C2C12 myoblasts in a co-axial system with and without pluronic as a confinement material. After 24 h, the percentage of viable cells in the co-axial system using pluronic has been slightly reduced to 80%; however, without using pluronic the viability was much lower after the same time, reaching almost 50%.

3.3.3. Contraction force evaluation of skeletal muscle bioactuators

The functionality of the muscle tissues is evaluated in terms of contractile behavior and assessed to understand whether the creation of a more biomimetic muscle tissue with a hierarchical structure will impact on the resulting force output. Figure 5(A) shows a schematic of the two-post system used as a force measurement platform (i), where the bending of the post due to the force contraction of the muscle is video-tracked (ii) and analyzed (iii) to obtain the post displacement graphs, where (iv) the single-twitch contractions of tissue were observed (movie S2). Then, the Euler–Bernoulli beam bending equation was used to correlate the displacement with the contraction force (more details are provided in the Materials and Methods section). Force measurements revealed that the muscle tissues fabricated by PACA-3D printing presented higher force output throughout the experimental timeline, especially on day 12, when a three times stronger contraction force was obtained (figure 5(B) and movie S3). This significant increase in force output suggests that the fabrication of hierarchically organized muscle tissue enhanced myotube maturation, which could be related to improved sarcomere remodeling during contraction [59]. The effects of several variables, such as the number of printed filaments, differentiation day, printing approach, or filament size, which directly affect the muscle tissue force generation, were analyzed using a linear mixed effects model (figures 5(C)–S7). We performed a linear mixed-effect model analysis to determine the individual effects of different parameters on the final bioactuator output force, specifically, the type of bioprinting, differentiation day, and number of printed layers. The mixed-effect model is suitable for this type of experimental design, as it takes into account both fixed effects (those parameters that are controlled and manipulated) and random effects (those that are not controlled but can influence the outcome, such as sample-to-sample variability), which are common

when dealing with biological samples. In our experimental setup, we tested different sources of random effects (or random variability) in our samples: (i) from the sample ID (each individual sample), (ii) cell passage (always 3 or 4), and (iii) printing ID (set of samples that were printed on the same day). We evaluated these three models (table S1), and among them, the model accounting for variability in sample ID outperformed the others both in terms of explaining the between-group variance (with an intraclass correlation coefficient of 0.45) and the overall variance (with an R^2 of 0.63). Thus, approximately 45% of the variance in the logarithm of the force output can be attributed to differences between the samples, and the model overall accounted for 63% of the variability the logarithm of the force. Therefore, we deduced that the cell passage (at least between passages 3 and 4) and printing day did not significantly influence the force output of the bioactuators, but sample-to-sample variability was.

Our final linear mixed model was thus described as:

$$\log(F)_i = \beta_0 + \beta_1 \cdot D_i + \beta_2 \cdot T_i + \beta_3 \cdot L_i + b_{0i} + b_{1i} \cdot D_i + \varepsilon_i,$$

where $\log(F)_i$ represents the logarithm of the force for sample i, β are the model fixed effect coefficients, D_i is the differentiation day, T_i is the type of printing (where 0 is the conventional printing, the baseline, and 1 is PACA-3D printing), L_i is the number of layers, b_{0i} and b_{1i} are the random intercept and random slope for each day (respectively) associated to sample i, and $\in_i$ is the residual error. In this model, we not only allowed for a random effect in the intercepts of the model to account for sample-to-sample variability, but also for a random slope for the differentiation day, to account for the fact that different samples might follow slightly different differentiation patterns as days pass. The results of the model are shown in tables S2 and S3, and the model diagnostics in figure S7 demonstrate that the data and model fulfill the assumptions of normality and homoscedasticity.

Figure 5(C) shows the size effect (after exponentiating to improve interpretation; see table S3) of three fixed effects: differentiation day, number of layers, and type of bioprinting. It could be expected that including more layers in the construct would lead to a higher force output; however, the results indicated otherwise. Printing more layers had a small, albeit negative, effect on the force, which was not statistically significant; for each layer, the model estimated a reduction of force output by a factor of 0.83. This suggests that muscle tissues with wider diameters could still suffer from poor nutrient diffusion to the interior due to filament fusion after printing (see figures 4(B) and S8(C)), causing apoptosis or reduced differentiation. Although our method can prevent the fusion of filaments during crosslinking and thus potentially improve the differentiation of the fibers, it cannot avoid the fusion of filaments during differentiation. Therefore, the addition of more filaments to the bioactuator does not seem to increase the force output, as expected. However, using the PACA-3D printing method, compared to the conventional method, produced a significant improvement in the force output. Using the PACA-3D method resulted in an average of 2.6 times more force, which was statistically significant, with a large confidence interval that was skewed towards even higher values. As expected, the differentiation day also increased the force output by a factor of 1.2 per day. Therefore, the results presented here show that there is a great advantage in using the PACA-3D method to achieve stronger muscle tissue, which is of great interest not only in the bioengineering field but also in providing relevant muscle models useful as drug screening platforms for various muscle-related diseases [11].

3.3.4. Biological characterization of skeletal muscle bioactuators

As previously mentioned, to have functional contractile muscle tissue, it is necessary to ensure correct cell differentiation and the formation of myotubes by myoblast fusion (figure 6(A). Given the demonstrated positive impact of PACA-3D on tissue performance, we further evaluated the degree of tissue differentiation and maturation real-time quantitative polymerase chain reaction (RT-qPCR) and using fluorescence microscopy, as shown in figures 6 and 7, respectively. The expression of myogenic markers (i.e. MyoD and Myogenin), as well as maturation-related genes associated with Myosin Heavy Chain (i.e. MyHCI, MyHCIIa, MyHCIIb, and MyHCIIx), was evaluated at days 0, 4, 9, and 12 of differentiation. Generally, the gene expression patterns observed in figure 6(B), correlate with our previous publications [10, 41]. For instance, downregulation over time of the myoblast marker MyoD indicates the differentiation of these cells into myocytes and myotubes. The typical peak in the expression of Myogenin, a myocyte marker gene, was also observed on day 4, however its levels in PACA-3D remained consistently higher than those in conventional samples throughout the entire differentiation period. In mature skeletal muscle tissues, there are two types of fibers: slow-twitch and fast-twitch fibers, also known as type I and type II, respectively. MyHCI is associated with slow contraction speed (i.e. low ATP-ase activity) but provides resistance to fatigue, while the MyHCIIa isoform is related to higher twitch speeds (i.e. high ATP-ase activity) that present less fatigue resistance [60]. Therefore, the functionality of skeletal muscles depends on the amount of different fiber types found in the tissue. Interestingly, a significant peak in the expression of all tested MyHCII subtypes on day 9 was observed in PACA-3D tissues,

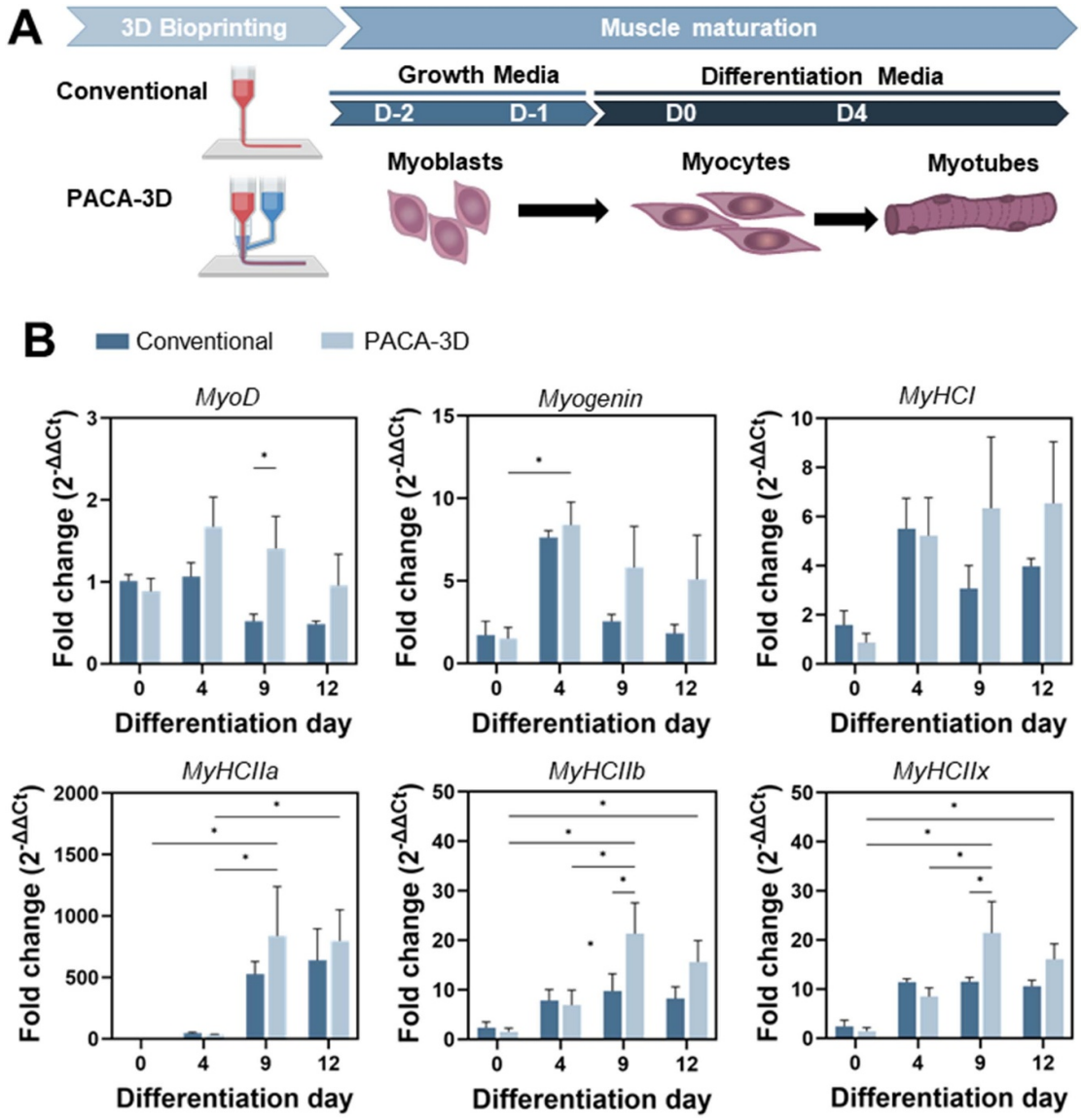

Figure 6. Characterization of myogenic marker gene expression in skeletal muscle bioactuators using PACA-3D and conventional bioprinting. (A) Timeline of the differentiation process of the 3D bioprinted skeletal muscle bioactuators. (B) Gene expression analysis by RT-qPCR of the differentiation process of bioprinted muscle actuators. All values are represented as mean ± SEM. Statistical significance was assessed using a two-way analysis of variance (ANOVA) followed by Tukey's multiple comparisons test ($p < 0.05(*)$). Absence of pairwise comparison indicates non-significant differences. Created in BioRender. Sánchez (2025) https://BioRender.com/dzrgt7a.

with levels higher than those in conventional tissues. In contrast, levels of MyHCIIb and -x remained constant in conventional tissues after their up regulation at day 4, while MyHCIIa showed a slight increase by day 12. Focusing on MyHCI expression, although there was no statistical difference between the muscle tissues fabricated with PACA-3D and conventional printing, probably due to the high variability between samples, we observed a notable up regulation at day 4. In conventional samples, this marked the peak of expression, whereas in PACA-3D tissues, expression levels showed a gradual increase on days 9 and 12. These results provide insight into the differences in myosin composition between samples and suggest a greater presence of both slow- and fast-type myosin in PACA-3D, which may explain the higher forces observed in these samples.

To further assess the differentiation process at the protein level, we stained key myogenic markers (MyoD and Myogenin) in tissue cryosections as shown in figures 7 and S8. In both PACA-3D and conventional samples, we observed a notable decrease in MyoD- and Myogenin-positive cells from day 0 to day 4, with levels remaining low throughout the rest of the differentiation period, suggesting myoblast and myocyte differentiation into myofibers. However, PACA-3D samples showed a significant increase in MyoD+ and Myogenin+ cells at day 0 compared to conventional samples (figure 7(A)). Indeed, the reduction in MyoD+ cells from day 0 to day 4 was more

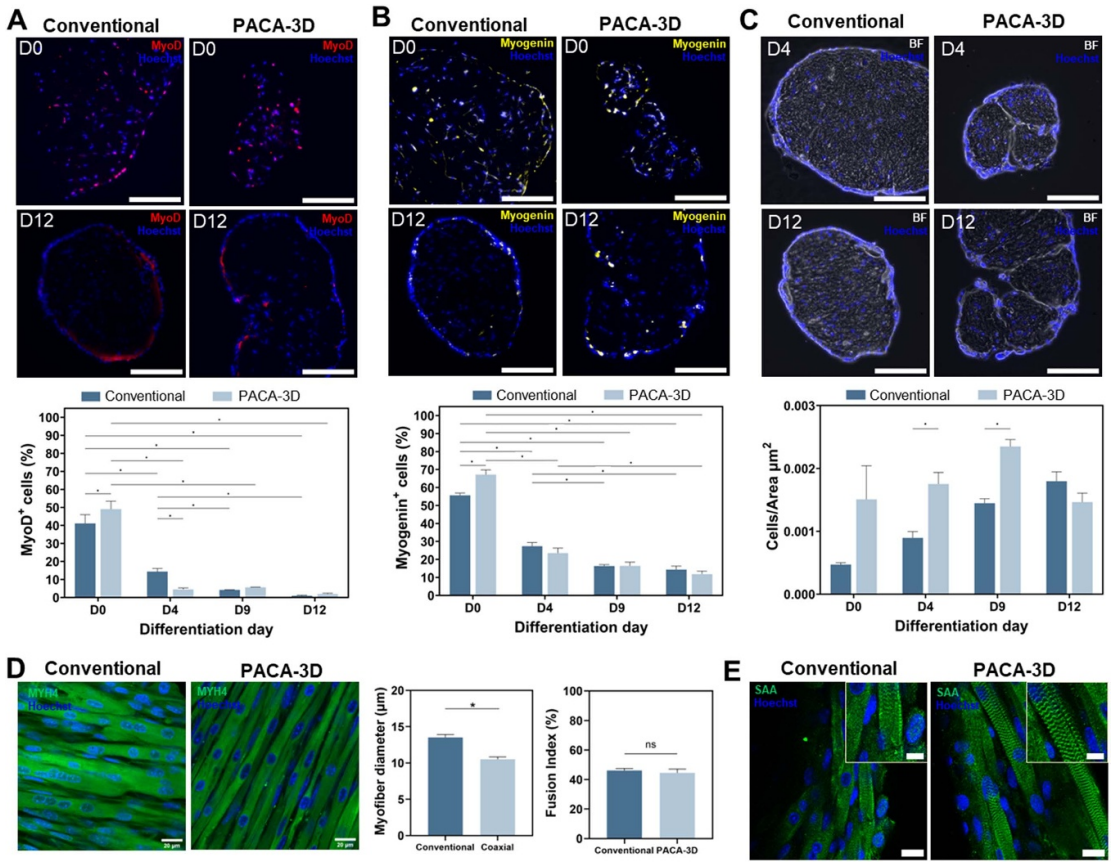

Figure 7. Characterization of immunofluorescence staining of myogenic markers in skeletal muscle bioactuators using PACA-3D and conventional bioprinting. D0 to D12 indicate differentiation days (two days after printing), as displayed in figure 5. (A) Immunostaining images and quantification of MyoD expression in cryosectioned muscle tissues at different time points. (B) Immunostaining images and quantification of Myogenin expression in cryosectioned muscle tissues at different time points. Scale bar: 200 μm. All values are represented as mean $\pm$ SEM. Statistical significance was assessed using a two-way analysis of variance (ANOVA) followed by Tukey's multiple comparisons test ($p < 0.05(^*)$. Absence of pairwise comparison indicate non-significant differences. (C) Microscope images and quantification from cryosectioned bioactuators at various differentiation days showing the increment of nucleus (Hoechst) number and organization at the edges of the filaments (visualized with bright field (BF). Scale bar: 200 μm. All values are represented as mean $\pm$ SEM. Statistical significance was assessed using an unpaired multiple t-test ($p < 0.05(^*)$. Absence of pairwise comparison indicate non-significant differences. (D) Immunostaining of myosin 4 (MHY4) after 12 d of differentiation of both conventional and PACA-3D bioactuators. Scale bar: 20 μm. Graphs display the differences in myotube diameter and fusion index between samples. Statistical significance was assessed using an unpaired t-test. (E) Immunostaining of sarcomeric alpha actinin at differentiation day 12. Scale bar: 20 μm.

pronounced in PACA-3D tissues. This, along with the higher cell density per area observed in PACA-3D (figures 7(C) and S8(C)), suggests that our approach enhances early-stage differentiation and promotes cell proliferation. We hypothesize that this effect results from increased oxygen and nutrient flow, facilitated by the individual thin filaments created with our technique. While these filaments eventually compact into a dense structure, their individual nature remains visible, unlike the fully fused filaments observed in conventional bioprinting. This physical separation likely supports continued differentiation through day 12, as shown in figure S8, where bright-field images clearly reveal the edges of individual filaments within the final compact structure. Notably, in all samples, we observed cell migration from the center of the 3D constructs toward the outer layers. This migration was likely driven by the cells tendency to move closer to the cell medium, with the presence of medium supplements like IGF-1 potentially enhancing this migration through its chemotactic effects [61]. When comparing RT-qPCR and immunostaining quantifications, both methods showed a reduction of MyoD and Myogenin expression over time. However, slight differences in expression levels were observed, with immunostaining revealing a significant decrease in protein levels at day 4, while mRNA levels remained relatively higher. This discrepancy may simply reflect the limitations of immunofluorescence quantification, therefore further validation using additional protein quantification techniques could be done in the future.

Figure 7(D) shows the immunofluorescence staining of myosin 4, also known as MyHCIIb, and cell nuclei (Hoechst) performed on day 12 of differentiation. Highly aligned multinucleated fibers were obtained in both types of samples, demonstrating proper muscle maturation. This was also

reflected in the myotube alignment, evaluated by the angle dispersion of myotubes after a FFT of a set of immunofluorescence images (figure S9). Myotubes in conventionally printed samples are significantly wider, which is normally correlated with muscular hypertrophy [62]. It is unclear, however, whether the same level of hypertrophy can be obtained in lab-grown skeletal muscle tissue, especially since they do not contain satellite cells, which play a major role in muscle regeneration and maintenance and contribute to the development of hypertrophic muscles when needed (i.e. after exercise) [63–66]. Previous reports shown that the strongest tissue constructs generated in absence of satellite cells were thinner [43, 67, 68]. Then, it is possible that myotubes organization during the spreading phase are able to elongate the tissues but not grow them wider, as the repair and growth mechanism mediated by satellite cells cannot take place. Moreover, not significant differences were found in the values of fusion index which indicates that fusion of myocytes into multinucleated myotube occurs at a similar rate in both conventional and PACA-3D samples. Remarkably, we observed distinct differences in sarcomeric structure formation, as shown by the staining of sarcomeric α-actinin in figure 7(E). While myotubes with sarcomere formation could be observed in both samples type, PACA-3D tissues showed a greater number of myotubes with well-organized and more visually defined sarcomere as shown in a set of images from figure S10. Given that the sarcomere is the fundamental contractile unit of muscle fibers and essential for proper muscle contraction [69], these findings may also explain why PACA-3D tissues generated a threefold higher force output compared to conventional samples. Taken together, these findings suggest that the higher expression levels of MyHCII subtype genes, the increased presence of MyoD- and Myogenin-positive cells during early differentiation, and the enhanced sarcomere organization observed in PACA-3D may explain the generation of stronger forces. However, since PACA-3D resulted in thinner myotubes, it is difficult to conclude that our printing approach directly enhances muscle maturation, and further research is needed to prove this aspect. Nevertheless, it supports the formation of muscle fibers with improved functionality, demonstrating the potential of this method for fabricating skeletal muscle bioactuators.

4. Conclusions

The PACA-3D hereby presented represents a novel and versatile approach to obtain individual bioengineered filaments with well-controlled homogeneity and width. Such individual filaments are of great interest for tissue engineering purposes, generating a functional fascicle-like structure that resembles the complexity of the native skeletal muscle tissue architecture. We explored two main hydrogel confinement methods: the first was based on chemical crosslinking of alginate upon extrusion owing to the presence of CaCl2 within pluronic, and the second was based on physical repulsion between jellified gelatin and pluronic. Both strategies can be used in combination with any kind of biopolymer, such as fibrinogen, Matrigel, and GelMA, making PACA-3D a universal 3D bioprinting method.

We demonstrated that our technology allows the fabrication of filaments of approximately 200 μm, which corresponds to the oxygen diffusion limit and does not fuse during the extrusion process. These filaments showed important advantages in the fabrication of skeletal muscle-based bioactuators compared to conventional extrusion-based 3D bioprinting. Probably due to the enhanced oxygen and nutrient diffusion, the myofibers obtained by PACA-3D showed increased expression of MyHC genes and clearly advanced sarcomere organization, resulting in 3 times stronger than that of conventional bioactuators. This bioprinting technique presents a new strategy for skeletal muscle bioengineering, without the need for a sacrificial bath that often limits scalability and printing flexibility, providing a versatile tool that paves the way towards improved biomimetic models for basic developmental research and biomedical applications.

Data availability statement

All data that support the findings of this study are included within the article (and any supplementary files).

Acknowledgment

R.M. would like to thank the UK Research and Innovation (UKRI) for funding (grant refs ES/X006255/1 and MR/S032711/1). M. G. acknowledges the financial support from the Spanish Ministry of Science through Ramon y Cajal Grant No. RYC2020-945030119-I. and Unidades de Excelencia María de Maeztu» 2021 CEX2021-001202-M. J.F. and SS acknowledge financial support from the European Union's Horizon Europe research and innovation program under grant agreement No. 101070328 (Biomeld). S.S. acknowledges CERCA program by the Generalitat de Catalunya, the Secretaria d'Universitats i Recerca del Departament d'Empresa i Coneixement de la Generalitat de Catalunya through the project 2021 SGR 01606, and the 'Centro de Excelencia Severo Ochoa', funded by Agencia Estatal de Investigación (CEX2018-000789-S). N.R. is thankful for financial support from the Spanish Ministry of Science (Predoctoral fellowship PRE2019-088801 and Grants PID2021-128417OB-I00 and RETI2018-098164-B-I00 funded by MCIN/AEI/10.13039/501100011033).

T.P. thanks the Irène Curie Fellowship for their assistance. D.E.U. is grateful to the Spanish Ministry of Science for financial support through the project PID2021-128417OB-I00, funded by MCIN/AEI/10.13039/501100011033, and co-funded by 'ERDF—A Way of Making Europe' and the European Union Next Generation EU/PRTR. This project has received also funding from the European Research Council (ERC) under the European Union's Horizon 2020 and Horizon Europe research and innovation programmes (grants agreement No 866348, i-NanoSwarms).

Ethical Compliance

Not applicable, as only commercial cell lines have been used for the development of the skeletal muscle bioactuators.

Conflict of interest

The authors declare no conflict of interest.

ORCID iDs

Judith Fuentes https://orcid.org/0000-0003-2639-6907
Rafael Mestre https://orcid.org/0000-0002-2460-4234
Maria Guix https://orcid.org/0000-0002-5219-6434
David Esporrín-Ubieto https://orcid.org/0000-0002-9858-415X
Ibtissam Ghailan Tribak https://orcid.org/0000-0001-7953-2744
Noelia Ruiz-González https://orcid.org/0000-0002-2467-331X
Tania Patiño https://orcid.org/0000-0001-9979-7926
Samuel Sánchez https://orcid.org/0000-0001-9713-9997

References

[1] Murphy S V and Atala A 2014 3D bioprinting of tissues and organs *Nat. Biotechnol.* **32** 773–85
[2] Donderwinkel I *et al* 2017 Bio-inks for 3D bioprinting: recent advances and future prospects *Polym. Chem.* **31** 7250–6
[3] Kang H-W, Lee S J, Ko I K, Kengla C, Yoo J J and Atala A 2016 A 3D bioprinting system to produce human-scale tissue constructs with structural integrity *Nat. Biotechnol.* **34** 312–9
[4] Zhang Y S, Haghiashtiani G, Hübscher T, Kelly D J, Lee J M, Lutolf M, McAlpine M C, Yeong W Y, Zenobi-Wong M and Malda J 2021 3D extrusion bioprinting *Nat. Rev. Methods Primers* **1** 75
[5] Pati F, Jang J, Ha D, Kim S W, Rhie J, Shim J, Kim D and Cho D 2014 Printing three-dimensional tissue analogues with decellularized extracellular matrix bioink *Nat. Commun.* **5** 1–11
[6] Kim Y B, Lee H and Kim G H 2016 Strategy to achieve highly porous/biocompatible macroscale cell blocks, using a collagen/genipin-bioink and an optimal 3D printing process *ACS Appl. Mater. Interfaces* **8** 32230–40
[7] Lee B H, Lum N, Seow L Y, Lim P Q and Tan L P 2016 Synthesis and characterization of types A and B gelatin methacryloyl for bioink applications *Materials* **9** 1–13
[8] Shor L, Güçeri S, Chang R, Gordon J, Kang Q, Hartsock L, An Y and Sun W 2009 Precision extruding deposition (PED) fabrication of polycaprolactone (PCL) scaffolds for bone tissue engineering *Biofabrication* **1** 015003
[9] Lind J U *et al* 2017 Instrumented cardiac microphysiological devices via multimaterial three-dimensional printing *Nat. Mater.* **16** 303–8
[10] Mestre R, Patiño T, Barceló X, Anand S, Pérez-jiménez A and Sánchez S 2019 Force modulation and adaptability of 3D-bioprinted biological actuators based on skeletal muscle tissue *Adv. Mater. Technol.* **4** 1800631
[11] Mestre R, García N, Patiño T, Guix M, Fuentes J, Valerio-Santiago M, Almiñana N and Sánchez S 2021 3D-bioengineered model of human skeletal muscle tissue with phenotypic features of aging for drug testing purposes *Biofabrication* **13** 045011
[12] Xu Y, Hu Y, Liu C, Yao H, Liu B and Mi S 2018 A novel strategy for creating tissue-engineered biomimetic blood vessels using 3D bioprinting technology *Materials* **11** 1581
[13] Filippi M, Yasa O, Giachino J, Graf R, Balciunaite A, Stefani L and Katzschmann R K 2023 Perfusable biohybrid designs for bioprinted skeletal muscle tissue *Adv. Healthcare Mater.* **12** 2300151
[14] Dufaud M, Solé L, Maumus M, Simon M, Perrier-Groult E, Subra G, Jorgensen C and Noël D 2022 3D bioprinting of articular cartilage: recent advances and perspectives *Bioprinting* **28** e00253
[15] Yan Y *et al* 2024 3D bioprinting of human neural tissues with functional connectivity *Cell Stem Cell* **31** 260–274.e7
[16] Ahrens J H, Uzel S G M, Skylar-Scott M, Mata M M, Lu A, Kroll K T and Lewis J A 2022 Programming cellular alignment in engineered cardiac tissue via bioprinting anisotropic organ building blocks *Adv. Mater.* **34** 2200217
[17] Weng T *et al* 2021 3D bioprinting for skin tissue engineering: current status and perspectives *J. Tissue Eng.* **12** 204173142110285
[18] Merceron T K, Burt M, Seol Y-J, Kang H-W, Lee S J, Yoo J J and Atala A 2015 A 3D bioprinted complex structure for engineering the muscle–tendon unit *Biofabrication* **7** 035003
[19] Lee J, Lee H, Jin E-J, Ryu D and Kim G H 2023 3D bioprinting using a new photo-crosslinking method for muscle tissue restoration *npj Regen. Med.* **8** 18
[20] Fornetti E *et al* 2023 A novel extrusion-based 3D bioprinting system for skeletal muscle tissue engineering *Biofabrication* **15** 025009
[21] Akiyama Y, Nakayama A, Nakano S, Amiya R and Hirose J 2021 An electrical stimulation culture system for daily maintenance-free muscle tissue production *Cyborg. Bionic Syst.* **2021** 1–12
[22] Rouwkema J, Koopman B F J M, van Blitterswijk C A V, Dhert W J A and Malda J 2009 Supply of nutrients to cells in engineered tissues *Biotechnol. Genet. Eng. Rev.* **26** 163–78
[23] Cvetkovic C, Raman R, Chan V, Williams B J, Tolish M, Bajaj P, Sakar M S, Asada H H, Saif M T A and Bashir R 2014 Three-dimensionally printed biological machines powered by skeletal muscle *Proc. Natl Acad. Sci.* **111** 10125–30
[24] Neal D, Sakar M S, Ong L-L S and Harry Asada H 2014 Formation of elongated fascicle-inspired 3D tissues consisting of high-density, aligned cells using sacrificial outer molding *Lab. Chip* **14** 1907–16
[25] Chen S, Nakamoto T, Kawazoe N and Chen G 2015 Engineering multi-layered skeletal muscle tissue by using 3D microgrooved collagen scaffolds *Biomaterials* **73** 23–31

[26] Zhang Y, Zhang Z, Wang Y, Su Y and Chen M 2020 3D myotube guidance on hierarchically organized anisotropic and conductive fibers for skeletal muscle tissue engineering *Mater. Sci. Eng. C* **116** 111070
[27] Kim K, Jin S and Shin M 2024 Effect of 3D-Printable anisotropic fibrous hydrogels on fabricating artificial skeletal muscle constructs *Adv. Ther.* **7** 2300170
[28] Homan K A, Kolesky D B, Skylar-Scott M A, Herrmann J, Obuobi H, Moisan A and Lewis J A 2016 Bioprinting of 3D convoluted renal proximal tubules on perfusable chips *Sci. Rep.* **6** 34845
[29] Lee A, Hudson A R, Shiwarski D J, Tashman J W, Hinton T J, Yerneni S, Bliley J M, Campbell P G and Feinberg A W 2019 3D bioprinting of collagen to rebuild components of the human heart *Science* **365** 482–7
[30] Liu W, Zhong Z, Hu N, Zhou Y, Maggio L, Miri A K, Fragasso A, Jin X, Khademhosseini A and Zhang Y S 2018 Coaxial extrusion bioprinting of 3D microfibrous constructs with cell-favorable gelatin methacryloyl microenvironments *Biofabrication* **10** 024102
[31] Millik S C, Dostie A M, Karis D G, Smith P T, McKenna M, Chan N, Curtis C D, Nance E, Theberge A B and Nelson A 2019 3D printed coaxial nozzles for the extrusion of hydrogel tubes toward modeling vascular endothelium *Biofabrication* **11** 045009
[32] Shyam Mohan T, Datta P, Nesaei S, Ozbolat V and Ozbolat I T 2022 3D coaxial bioprinting: process mechanisms, bioinks and applications *Prog. Biomed. Eng.* **4** 022003
[33] Lee H, Kim S H, Lee J S, Lee Y J, Lee O J, Ajiteru O, Sultan M T, Lee S W and Park C H 2023 Functional skeletal muscle regeneration using muscle mimetic tissue fabricated by microvalve-assisted coaxial 3D bioprinting *Adv. Healthcare Mater.* **12** 2202664
[34] Duong V T, Dang T T, Le V P, Le T H, Nguyen C T, Phan H L, Seo J, Lin C-C, Back S H and Koo K 2025 Direct extrusion of multifascicle prevascularized human skeletal muscle for volumetric muscle loss surgery *Biomaterials* **314** 122840
[35] Celikkin N *et al* 2023 Combining rotary wet-spinning biofabrication and electro-mechanical stimulation for the *in vitro* production of functional myo-substitutes *Biofabrication* **15** 045012
[36] Costantini M *et al* 2021 Biofabricating murine and human myo-substitutes for rapid volumetric muscle loss restoration *EMBO Mol. Med.* **13** e12778
[37] Raman R, Grant L, Seo Y, Cvetkovic C, Gapinske M, Palasz A, Dabbous H, Kong H, Pinera P P and Bashir R 2017 Damage, healing, and remodeling in optogenetic skeletal muscle bioactuators *Adv. Healthcare Mater.* **6** 1700030
[38] Sakar M S, Neal D, Boudou T, Borochin M A, Li Y, Weiss R, Kamm R D, Chen C S and Asada H H 2012 Formation and optogenetic control of engineered 3D skeletal muscle bioactuators *Lab. Chip* **12** 4976–85
[39] Sun Y, Duffy R, Lee A and Feinberg A W 2013 Lee A and Feinberg A W 2013 Optimizing the structure and contractility of engineered skeletal muscle thin films *Acta Biomater.* **9** 7885–94
[40] Tejedera-Villafranca A, Montolio M, Ramón-Azcón J and Fernández-Costa J M 2023 Mimicking sarcolemmal damage *in vitro*: a contractile 3D model of skeletal muscle for drug testing in Duchenne muscular dystrophy *Biofabrication* **15** 045024
[41] Mestre R, Fuentes J, Lefaix L, Wang J, Guix M, Murillo G, Bashir R and Sánchez S 2023 Improved performance of biohybrid muscle-based bio-bots doped with piezoelectric boron nitride nanotubes *Adv. Mater. Technol.* **8** 2200505
[42] Morimoto Y, Onoe H and Takeuchi S 2020 Biohybrid robot with skeletal muscle tissue covered with a collagen structure for moving in air *APL Bioeng.* **4** 026101
[43] Kim Y *et al* 2023 Remote control of muscle-driven miniature robots with battery-free wireless optoelectronics *Sci. Robot.* **8** eadd1053
[44] Zhuang P, An J, Chua C K and Tan L P 2020 Bioprinting of 3D *in vitro* skeletal muscle models: a review *Mater. Des.* **193** 108794
[45] Brooks S V, Guzman S D and Ruiz L P 2023 Skeletal muscle structure, physiology Handb Clin Neurol. **195** 3–16
[46] Lieber R L 2022 *Skeletal muscle structure, function, and plasticity* (Lippincott Williams & Wilkins)
[47] Yeo M G, Lee J-S, Chun W and Kim G H 2016 An innovative collagen-based cell-printing method for obtaining human adipose stem cell-laden structures consisting of core-sheath structures for tissue engineering *Biomacromolecules* **17** 1365–75
[48] Wu W, Deconinck A and Lewis J A 2011 Omnidirectional printing of 3D microvascular networks *Adv. Mater.* **23** 178–83
[49] Pi Q *et al* 2018 Digitally tunable microfluidic bioprinting of multilayered cannular tissues *Adv. Mater.* **30** 1706913
[50] Hong S, Kim J S, Jung B, Won C and Hwang C 2019 Coaxial bioprinting of cell-laden vascular constructs using a gelatin-tyramine bioink *Biomater. Sci.* **7** 4578–87
[51] Amirrah I N, Lokanathan Y, Zulkiflee I, Wee M F M R, Motta A and Fauzi M B 2022 A comprehensive review on collagen Type I development of biomaterials for tissue engineering: from biosynthesis to bioscaffold *Biomedicines* **10** 2307
[52] Sonaye S Y, Ertugral E G, Kothapalli C R and Sikder P 2022 Extrusion 3D (Bio)printing of alginate-gelatin-based composite scaffolds for skeletal muscle tissue engineering *Materials* **15** 7945
[53] Raman R, Cvetkovic C and Bashir R 2017 A modular approach to the design, fabrication, and characterization of muscle-powered biological machines *Nat. Protocols* **12** 519–33
[54] Jia W *et al* 2016 Direct 3D bioprinting of perfusable vascular constructs using a blend bioink *Biomaterials* **106** 58–68
[55] Yin J, Yan M, Wang Y, Fu J and Suo H 2018 3D bioprinting of low-concentration cell-laden Gelatin methacrylate (GelMA) bioinks with a two-step cross-linking strategy *ACS Appl. Mater. Interfaces* **10** 6849–57
[56] Kjar A *et al* 2024 Biofunctionalized gelatin hydrogels support development and maturation of iPSC-derived cortical organoids *Cell Rep.* **43** 114874
[57] Fonkwe L G, Narsimhan G and Cha A S 2003 Characterization of gelation time and texture of gelatin and gelatin–polysaccharide mixed gels *Food Hydrocoll.* **17** 871–83
[58] Koch L, Saha S and Huber K 2024 Impact of temperature on the self-assembly of fibrinogen in thrombin-free solutions *J. Phys. Chem. Lett.* **15** 9987–93
[59] Franchi M V, Reeves N D and Narici M V 2017 Skeletal muscle remodeling in response to eccentric vs. concentric loading: morphological, molecular, and metabolic adaptations *Front. Physiol.* **8** 447
[60] Plotkin D L, Roberts M D, Haun C T and Schoenfeld B J 2021 Muscle fiber type transitions with exercise training: shifting perspectives *Sports* **9** 127
[61] Xu B, Zhang M, Perlingeiro R C R and Shen W 2019 Skeletal muscle constructs engineered from human embryonic stem cell derived myogenic progenitors exhibit enhanced contractile forces when differentiated in a medium containing EGM-2 supplements *Adv. Biosyst.* **3** 1900005
[62] Fukada S and Ito N 2021 Regulation of muscle hypertrophy: involvement of the Akt-independent pathway and satellite cells in muscle hypertrophy *Exp. Cell Res.* **409** 112907
[63] Bazgir B, Fathi R, Valojerdi M R, Mozdziak P and Asgari A 2016 Satellite cells contribution to exercise mediated muscle hypertrophy and repair *Cell J.* **18** 473–84

[64] Fukada S, Akimoto T and Sotiropoulos A 2020 Role of damage and management in muscle hypertrophy: different behaviors of muscle stem cells in regeneration and hypertrophy *Biochim. Biophys. Acta* **1867** 118742
[65] Kaczmarek A, Kaczmarek M, Ciałowicz M, Clemente F M, Wolański P, Badicu G and Murawska-Ciałowicz E 2021 The role of satellite cells in skeletal muscle regeneration—the effect of exercise and age *Biology* **10** 1056
[66] Fukada S, Higashimoto T and Kaneshige A 2022 Differences in muscle satellite cell dynamics during muscle hypertrophy and regeneration *Skelet. Muscle* **12** 17
[67] Morimoto Y, Onoe H and Takeuchi S 2018 Biohybrid robot powered by an antagonistic pair of skeletal muscle tissues *Sci.Robot.* **3** eaat4440
[68] Guix M, Mestre R, Patiño T, de Corato M, Fuentes J, Zarpellon G and Sánchez S 2021 Biohybrid soft robots with self-stimulating skeletons *Sci. Robot.* **6** 1–14
[69] Martin A A, Thompson B R, Davis J P, Vang H, Hahn D and Metzger J M 2022 Sarcomere dynamics revealed by a myofilament integrated FRET-based biosensor in live skeletal muscle fibers *Sci. Rep.* **12** 18116